Performance Analysis of NOMA Enabled Active RIS-aided MIMO Heterogeneous IoT Networks with Integrated Sensing and Communication

Abhinav Singh Parihar, Keshav Singh, *Member, IEEE*, Vimal Bhatia, *Senior Member, IEEE*, Chih-Peng Li, *Fellow, IEEE*, and Trung Q. Duong, *Fellow, IEEE*

***Abstract*—With the imminent arrival of 6G communication, the relevance of advanced technologies, such as multi-input multi-output (MIMO), non-orthogonal multiple access (NOMA), reconfigurable intelligent surfaces (RIS), and integrated sensing and communication (ISAC), has become prominent for plethora of Internet of Things (IoT) applications. However, integrating ISAC into a MIMO heterogeneous network (HetNets) necessitates reevaluating network performance in terms of outage probability and ergodic rates. This paper introduces a novel analytical framework for evaluating downlink transmissions in MIMO HetNets. The proposed framework considers independent homogeneous Poisson point processes (PPP) for spatial arrangement of the NOMA-enabled base stations (BSs) and users. BS in the t-th tier exploits superimposed NOMA signal for target sensing. Active RISs are considered to be distributed with homogeneous PPP and are used to mitigate blockage for UEs when the direct link from the BSs does not exist. The approximated and asymptotic outage probability expressions are derived for two distinct scenarios: one involving direct transmission from the BS to the typical blocked user and the other entailing transmission via active RIS. Moreover, a practical case of imperfect successive interference cancellation (i-SIC) is considered. The analysis emphasizes the benefits of the proposed active RIS-NOMA compared to conventional orthogonal multiple access HetNets, and valuable insights are drawn by varying the number of RIS elements. Additionally, an increase in the RIS elements significantly improves the proposed active RIS-NOMA outage performance. The approximated expressions of ergodic rates, system throughput and beampattern for the sensing performance are also derived.**

The work of K. Singh and C.-P. Li was supported in part by the National Science and Technology Council of Taiwan, under grants NSTC 112-2221-E-110-038-MY3, NSTC 113-2218-E-110-008, NSTC 112-2221-E-110-029-MY3 and in part by the Sixth Generation Communication and Sensing Research Center funded by the Higher Education SPROUT Project, the Ministry of Education of Taiwan. The work of V. Bhatia was supported in part by the IIITB COMET Foundation, established under the Advanced Communication Systems vertical of the National Mission on Interdisciplinary Cyber-Physical Systems (NM-ICPS) and in part by the MeitY's 13(28)/2020-CC&BT Scheme. The work of T. Q. Duong was supported in part by the Canada Excellence Research Chair (CERC) Program CERC-2022-00109.

A. S. Parihar, K. Singh, and C. P. Li are with the Institute of Communications Engineering, National Sun Yat-sen University, Kaohsiung 80424, Taiwan (Email: abhinavsingh2304@gmail.com, keshav.singh@mail.nsysu.edu.tw, cpli@mail.nsysu.edu.tw).

V. Bhatia is with Department of Electrical Engineering, Center for Advanced Electronics, Indian Institute of Technology Indore, Indore, 453552 India and Faculty of Informatics and Management, University of Hradec Kralove, 50003 Hradec Kralove, Czech Republic (e-mail:vbhatia@iiti.ac.in).

T. Q. Duong is with the Faculty of Engineering and Applied Science, Memorial University, St. John's, NL A1C 5S7, Canada, and with the School of Electronics, Electrical Engineering and Computer Science, Queen's University Belfast, BT7 1NN Belfast, U.K., and also with the Department of Electronic Engineering, Kyung Hee University, Yongin-si, Gyeonggi-do 17104, South Korea (e-mail: tduong@mun.ca).

***Index Terms*—Integrated sensing and communication, non-orthogonal multiple access, reconfigurable intelligent surfaces, stochastic geometry.**

I. Introduction

The emergence of Internet of Things (IoT) heralds a future where devices will autonomously communicate with each other, minimizing the need for direct human interaction [1]. This paradigm shift enables a multitude of applications, spanning smart cities [2], the Internet of Vehicles [3], and healthcare [4], and others. Leveraging cellular networks for IoT communications offers numerous advantages, facilitating a diverse array of IoT services. In the pursuit of meeting such escalating demand and accommodating the continuous surge in traffic, 6G wireless network architectures incorporate enabling technologies such as heterogeneous networks (HetNets), and multiple-input multiple-output (MIMO) [5]. To cope with the rapid growth in traffic, HetNets combines low-density high-power macro base stations (MBS) with denser low-power small base stations (SBS). However, the presence of severe co-tier and cross-tier interference poses challenges to practical deployment, resulting in a lower network throughput despite the spatial spectrum reuse gain utilized by HetNets to enhance network spectral efficiency [6].

Due to the unparalleled sensing demands inherent in forthcoming wireless networks, there is a discernible trend towards achieving the integration of wireless communication with radio sensing. Identifying a cost-effective and operationally viable solution within the existing network architecture constitutes a fundamental and pragmatic concern in the collaborative design of joint sensing and communication (S&C) [7]. Communication utilizes radio waves to transmit signals from a sender to a receiver, while sensing leverages radio frequency echoes scattered by a target. The analysis of these echoes involves extracting target parameters (e.g., target location, velocity, and size) using methods for example multiple signal classification and matched filtering, as well as learning-based approaches [8]. An achievable option involves making marginal modifications to the radio resource allocation within the existing communication system to support sensing capabilities [9]. Efficiently multiplexing signals from communication and sensing capacities to achieve harmony and compatibility relies on specifically adopted resource allocation strategies [10]. One such approach involves adjustments to allocate dedicated sensing signals in the time and frequency domains.

This results in the use of orthogonal resource multiplexing when combined with communication signals. [11] considered using NOMA to overlay S&C signals. In this scenario, the communication receiver utilizes prior information of the sensing signal and employs successive interference cancellation (SIC) at the receiver. This approach, termed integrated S&C (ISAC) by NOMA, complements the traditional orthogonal ISAC scheme. The fundamental concept behind ISAC is to enable both S&C seamlessly through a unified hardware architecture. This concept is motivated by the fact that S&C have the same principles, particularly reliance on radio waves. An interference management strategy was proposed in [11] to effectively tackle the complexities associated with the simultaneous reuse of communication and sensing resources, thereby minimizing the necessity of substantial changes to the existing communication systems. One approach involves concurrently executing communication and sensing operations within a wireless communication system by delivering the S&C signals onto the same resource block simultaneously.

A. Related works

Reconfigurable intelligent surfaces (RIS)-enabled wireless communications have garnered considerable interest, as illustrated in the works in [12]–[14]. The authors in [15] studied the channel characteristics within networks assisted by RIS. This evaluation involved the categorization of the space illuminated by the RIS. In [16], the authors introduced methodologies for maximizing energy efficiency with reduced complexity. These methodologies involves a joint design of transmit power and the configuration of phase shifts for the reflecting elements. In [17], the optimization of resource allocation for spectrally efficient RIS full-duplex was formulated under the framework of NOMA. [18] investigated performance of a full-duplex system employing Nakagami-m fading models. This system featured a full-duplex transceiver communicating for downlink and uplink, utilizing two separate RISs.

The outage probability and symbol error rate in wireless communications aided by RIS over Rayleigh fading channels were developed in [19]. Analyzing coverage probability performance under Nakagami-m channel conditions, [20] explored the moment generation functions for RIS-enabled systems. To assess the effect of line-of-sight (LoS) link, [21], [22] studied the outage probability, ergodic rate, and average symbol error of RIS-enabled networks over Rician fading. Beyond these contributions, [23] highlighted various application scenarios, including RIS implementation in simultaneous wireless information and power transfer. Two-way communications between users assisted by RIS, accounting for reciprocal or non-reciprocal channels, were evaluated in [24]. To address security concerns, [25] used the stochastic geometry to study average secrecy capacity and secrecy outage behaviours in RIS-aided networks.

A thorough review on integration of RISs and NOMA was provided in [26]. RIS-assisted NOMA networks have primarily revolved around performance analyses, as evidenced in works such as [27]–[29]. In [27], a straightforward design for the RIS-assisted NOMA was studied, demonstrating that the use of an increased amount of RIS elements reduces outage probability. [28] explored outage probability and ergodic rate of RIS-assisted NOMA networks considering both perfect and imperfect SIC. [29] studied the effect of coherent phase shifting on outage performance in RIS-NOMA networks. Advancing further, [30] studied the outage probability and ergodic rate for users in RIS-NOMA, achieved through the design of passive beamforming weights. NOMA with RIS was proposed in [31], aiming to maximize fairness among users. [32] investigated error probability and phase shift architecture for RIS-aided NOMA networks using imperfect SIC and group-based SIC schemes. Examining the outage characteristics in NOMA-assisted RIS with discrete phase shifting, [33] characterized scenarios based on a direct connection between the BS and users. For RIS-assisted NOMA and OMA, [34] investigated user rates to meet transmit power minimization challenges with discrete phases. Furthermore, [35] investigated the performance of RIS-supported NOMA networks, demonstrating the superior performance of RIS compared to full-duplex decode-and-forward (DF) relaying. In addition, [36] optimized the active and passive beamforming jointly at the BS and the RIS, respectively, to maximise the sum rate. In [37], the RIS-aided two-cell NOMA networks is considered, while [38] delved into phase shifting and power allocation, leveraging joint detection techniques.

The primary advantages of NOMA ISAC, encompassing resource efficiency, extensive compatibility, and flexibility, were demonstrated in [39]. The authors in [39] also analyzed the principal challenges associated with NOMA-ISAC uplink and downlink aspects. Research has been carried out for certain NOMA-ISAC techniques, such as spectrum allocation [40], sensing signal splitting and beamforming [41], and echo prediction [10]. These investigations assess the S&C capabilities utilizing information theory and estimation theory metrics. In contrast to the research above, [42] and [43] proposed an ISAC framework based on mutual information analysis. Introducing sensing mutual information as a potential criterion for sensing performance, the proposed framework establishes a universal lower bound on the estimation-theoretic metrics [43]. This approach offers a potential to streamline joint performance analysis and serves a consistent comprehension of ISAC. The works [39]–[43] are based on the passive RIS. However, the RIS can operate in both passive and active mode by adding a low-power amplifier to each reflecting element. Active RIS has received significant attention from academia and industry. Active RIS optimizes system capacity by adjusting the phase and amplitude of reflected signals [44]. In [44], the authors introduced a metasurface constructed using amplifiers that regulate electromagnetic waves in frequency and space domains. In [45], the multiplicative fading induced by passive RIS was alleviated by sacrificing power consumption on the active reflection element. Active RIS, while considerably more expensive than passive RIS due to its low-power amplifier, is still more affordable than other repeaters, such as amplify-and-forward (AF) and decode-and-forward (DF) relays. In [46], the author demonstrated that active RIS can convert passive RIS's double-fading path loss to additive form. Active RIS's subconnected topology allows independent regulation

for every element's phase shift [47]. Numerous studies have focused on RIS-aided ISAC as highlighted in [48] and [49]. Generally, two primary scenarios have been investigated for the RIS-aided ISAC system [50]. In the first scenario, direct BS-target links are utilized for sensing, with the RIS enhancing communication capabilities [51]–[53]. For instance, To reduce the transmit power of the base station in the presence of interference caused by the RIS, [51] jointly designed the active and passive beamforming matrices. Additionally, [52] addressed time sharing between S&C features and optimized the RIS phase shift, considering the sensing time. In the second scenario, the RIS is utilized to create a virtual link between the target and the base station, enhancing its advantages, especially in improving radar detection performance. Two main sensing performance metrics were considered in this context. By optimizing the beampattern at the target, the studies in [50], [54] ensured that the target received more focused signals for better sensing. In [55] and [56] sensors are installed in RIS for sensing. By utilizing the sensors to carry out the sensing task, this approach would lower the amount of hops and pathloss across the sensors and the BS. However, implementing this approach would complicate the hardware design and make it difficult to integrate with the existing communication protocols.

B. Motivation and contribution

The previous works discussed the application of NOMA to meet the growing demands for higher data rates, improved spectral efficiency, and enhanced network performance. They demonstrated significant potential in enhancing spectral efficiency, especially in networks supported by passive RISs. Despite these advantages, passive RISs inherently suffer from a double-path loss effect, which can limit their overall effectiveness. The study in [R1] has explored the use of active RIS to mitigate this double-path loss, showing promising improvements in performance. However, the integration of active RIS with NOMA remains under-explored, presenting an opportunity for further research to uncover potential benefits and optimizations. Moreover, the use of MIMO technology to perform ISAC in HetNets has not been thoroughly investigated. Moreover, to demonstrate the performance improvements brought by active RISs in HetNets, we develop an analytical framework using stochastic geometry specifically designed for MIMO systems. The novel contributions of this paper are:

- For downlink transmissions, we construct an analytical framework for MIMO HetNets employing RIS-aided NOMA-ISAC. This framework is based on stochastic geometry and assumes an independent homogeneous Poisson point process (PPP) for the distributions of base stations (BSs) and IoT user equipments (UEs). This framework uses active RISs to support the typical UE experiencing blockage.
- Approximated outage probability equations are derived for two distinct scenarios. Firstly, we consider that the link between the typical UE and the specified BS is blocked. In this instance, the typical user is served by the nearest RIS. Secondly, we explore a scenario with the BS serving the blocked user directly. In this instance, the typical user is served by the nearest BS.
- We conduct an extensive outage study on the typical user in the context of RIS-NOMA and RIS-OMA. Our results reveal that the outage probability in RIS-NOMA achieved improved performance than RIS-OMA. Additionally, there is enhancement in the outage performance of RIS-NOMA with a rise in the reconfigurable elements. Moreover, a practical case of imperfect successive interference cancellation (i-SIC) is considered at the receiver, making our system model more realistic.
- We derive asymptotic expressions for the outage probability of the typical user in the proposed RIS-NOMA networks. The asymptotic outage probability expressions provide insights into the diversity order.
- We assess the RIS-NOMA system throughput in the delay-limited mode. RIS-NOMA is shown to have a higher system throughput than RIS-OMA. Furthermore, the equations of ergodic rates are also derived.
- The sensing performance of RIS-NOMA in HetNets is characterized by calculating the BS received signal-to-interference-and-noise ratio (SINR) for sensing performance. The BS received SINR is plotted against transmit signal-to-noise ratio (SNR), which provides useful insights into the system behaviour under various transmit SNR conditions. The beampatern is also evaluated in the direction of the target. It is shown that increasing the quantity of reflecting elements in the active RIS can improve performance and lead to a smaller beam.

C. Paper organization

The structure of this paper is outlined as: Section II describes the system model. Section III is dedicated to deriving analytical outage probability expressions. Section IV derives analytical expressions of the ergodic rate. The beampattern analysis is provided in Section V. Section VI discusses the analytical as well as simulation results. Lastly, Section VII summarizes the key conclusions drawn from this study.

Notation: Bold small and capital letters signify vectors and matrices, respectively. The transpose and conjugate transpose operations are represented as $(\cdot)^T$ and $(\cdot)^H$, respectively. $\|\cdot\|$ and $|\cdot|$ represent the norm and absolute value operations, respectively. The expressions $\mathrm{Tr}(\mathbf{B})$ and $\mathrm{diag}(\mathbf{B})$ indicate the trace of the matrix $\mathbf{B}$ and the diagonal elements in a vector, respectively. The term $\mathcal{CN}(0,\sigma^2)$ refers to a complex circularly symmetric Gaussian random variable with zero mean and variance σ^2. $\mathbb{C}^{A\times B}$ represents $A\times B$ complex matrices. $\mathbb{E}[\cdot]$ represents the expectation operator. Additionally, $\mathbf{M}^{A\times B}$ denotes the matrix of dimension $A\times B$. $\mathbf{I}_N$ represents the $N\times N$ identity matrix. $\Pr[\mathcal{E}]$ denotes probability of occurring event $\mathcal{E}$.

II. System Model

We consider a two-tier downlink HetNet consisting of MBS and SBS as depicted in Fig. 1. Location of the BSs is based upon the independent homogeneous PPP denoted as Ω_t with

density λ_t such that $t \in \{m, s\}$, for MBS-tier and SBS-tier, respectively. The IoT UEs and targets are also distributed according to the PPP distribution denoted as Ω_u and Ω_t, respectively. It is considered that the BS of the t-th tier supports K-users on a single time-frequency resource block while sensing T-targets. The BS of the t-th tier consists of M_t transmit antennas and N_r receive antennas. It is considered that the RIS are at a fixed location from the BS. The users are also equipped with U_r receive antennas. It is assumed that $U_r \geq M_t$ this is because the future 6G networks will feature ultra-dense deployments of SBS, employing low-cost and low-power SBS [57]. Consequently, it is highly probable that such inexpensive SBSs will possess an equal or fewer number of antennas compared to the number of handsets to be served, especially considering the rapid advancement of capabilities in smartphones, tablets, and IoT devices. Cloud radio access networks exemplify another 6G application of the proposed approach, where users are served by a limited number of cost-effective remote radio heads to minimize fronthaul overhead. Additionally, the proposed approach can find application in IoT scenarios, such as smart homes, where the performance of a home BS mirrors that of laptops and other digital devices.

The calculation is conducted for a standard user randomly selected from Φ_u, by relocating the origin to the typical user's location. The designated BS that connects with this user is referred to as tagged BS. Specifically, to improve spectral efficiency, the BSs are enabled with NOMA, wherein the multiple UEs are grouped together and served in each orthogonal resource block. Every BS operates with open access, meaning a UE can attach to the BS based on the maximum power-based association scheme [58]. In the proposed work, a time-division approach is implemented to separate the S&C operations [40]. Specifically, the communication signal is transmitted during designated communication time slots, while the sensing signal is transmitted during separate sensing time slots.

A. Channel Model

1) Small-Scale Fading: It is considered that there is an absence of line-of-sight (LoS) between the BS-user link, hence the small-scale fading is considered to be Rayleigh-distributed. $\mathbf{W}_k$ represents the channel matrix of $U_r \times M_t$ dimension from BS to k-th user.

As line-of-sight connections are anticipated for the BS$\rightarrow$RIS link and the RIS$\rightarrow$UE link, the channels are characterized by Nakagami-m fading channels. BS$\rightarrow$RIS channels are represented by $\mathbf{H}_k$, an $R \times M_t$ matrix with the shape parameter as m_1. These gains correspond to the connection between the BS transmit antenna in the t-th tier and the r-th element of its associated RIS. The model for these channels is expressed as

$$\mathbf{H}_k = \begin{bmatrix} h_{1,1} & \cdots & h_{1,M_t} \\ \vdots & \ldots & \vdots \\ h_{R,1} & \cdots & h_{R,M_t} \end{bmatrix}. \tag{1}$$

The individual components of the fading is defined as $h_{r,n} \sim$ Nakagami$(m_1, 1)$.

The small-scale fading matrix between the RISs and user UE$_k$ is denoted as $\mathbf{G}_k$ is $(U_r \times R)$ matrix which also signifies Nakagami-m channel with the fading parameter m_2 governing the link between r-th element of designated RIS and u-th antenna of the UE$_k$. Similarly, as (7), the channel matrix for the RIS-user link is represented as

$$\mathbf{G}_k = \begin{bmatrix} g_{1,1} & \cdots & g_{1,R} \\ \vdots & \ldots & \vdots \\ g_{U_r,1} & \cdots & g_{U_r,R} \end{bmatrix}. \tag{2}$$

The individual components of the fading is defined as $g_{k,r} \sim$ Nakagami$(m_2, 1)$.

2) Large-scale path-loss: In scenarios where the dimensions of RIS elements are of a comparable scale with the wavelength, typically achieved by setting the length of RIS components to $1/4$ of the wavelength, these surfaces are regarded as diffuse scatterers, as discussed in [59]. Consequently, the path loss between BS at the t-th tier and the UE$_k$ be represented as:

$$L_{t,k} = \| r_{t,k} \|^{-\alpha_t}, \tag{3}$$

$$L_{t,r,k} = \| r_{t,r} \|^{-\alpha_t} \| r_{r,k} \|^{-\alpha_t}, \tag{4}$$

where $L_{t,k}$ represents the path loss between the t-th tier BS and the UE$_k$, while $L_{t,r,k}$ denotes the path loss between t-th tier BS and UE through the RIS. Distances for BS-UE$_k$, BS-RIS, and RIS-UE$_k$ links are denoted by $r_{t,k}$, $r_{t,r}$, and $r_{r,k}$, respectively. The phase-shift matrix $\mathbf{\Phi} = \sqrt{\Lambda}\text{diag}([e^{j\theta_1}, \ldots, e^{j\theta_r}, \ldots, e^{j\theta_R}])$ is introduced, following the notation from [60]. Here, $\theta_r \in [0, 2\pi)$ denotes the phase shift of the r-th element of the designated RIS. Λ represents the reflection amplification coefficient of active RIS. Each RIS is under the control of a dedicated controller, and these controllers can be interconnected, potentially through a wired backhaul, to synchronize phase-shift configuration across the system. Thanks to the electromagnetic scattering concept, every element reflects and amplifies the incoming RF signal with tunable amplitude and phase. As a result, active RIS is able to obtain a reflection amplification coefficient higher than one, i.e., $\Lambda > 1$ [45]. Actually, the incident signal can be amplified by a negative resistive device, such as a tunnel diode, which transforms the direct current bias into RF power.

B. Passive Beamforming Designs

The analysis is performed for a BS of t-th tier located at t_o. We begin by focusing on the signal model, where the signal vector at the BS, with dimensions $M_t \times 1$, is expressed as $\mathbf{s}_t = [a_1 s_1, \cdots, a_{M_t} s_{M_t}]^T$, where a_k is the power allocation coefficient for UE$_k$, such that $\sum_{k=1}^{M_t} a_k^2 = 1$. s_k is the symbol corresponding to UE$_k$. The users are grouped based on the channel state information as in [61], and [62]. The channel gains are ordered as $L_{t_0,r,1}|\mathbf{h}_{r,1}^H \mathbf{\Theta}_r \mathbf{h}_{t_0,r}|^2 \leq \cdots \leq L_{t_0,r,k}|\mathbf{h}_{r,k}^H \mathbf{\Theta}_r \mathbf{h}_{t_0,r}|^2 \leq \cdots \leq L_{t_0,r,K}|\mathbf{h}_{r,K}^H \mathbf{\Theta}_r \mathbf{h}_{t_0,r}|^2$, their corresponding power allocation coefficients are ordered as $a_1 \geq \cdots \geq a_k \geq \cdots \geq a_K$. Therefore, the receiver starts decoding the strongest signal and progressively cancels out interference from weaker signals based on their channel state information.

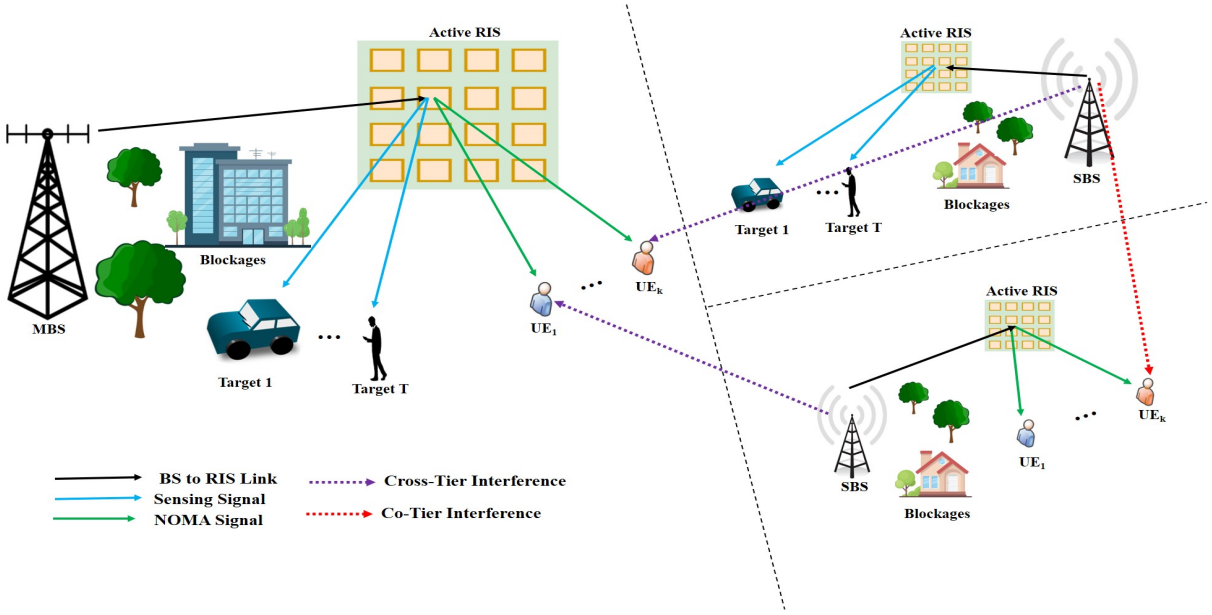

Fig. 1: Overview of the proposed system model comprising of MBS and SBS tier.

1) Communication from BS via RIS: While ensuring generality, we centre our focus on UE$_k$. The received signal from the designated BS and the RIS is expressed as

$$\mathbf{y}_k = \sqrt{\Lambda L_{t_0,r,k}}\mathbf{H}_k\boldsymbol{\Theta}\mathbf{G}_k\mathbf{D}\sqrt{P_t}\mathbf{s}_{t_0}(t) + \underbrace{\sum_{\substack{t\in\Phi_t\setminus t_0\\ t\in\{m,s\}}}\sqrt{P_t L_{t,k}}\mathbf{W}_{t,k}\mathbf{D}_t\mathbf{s}_t}_{\text{interference from other BSs}} + \mathbf{n}_k, \tag{5}$$

where P_t is the power transmitted by the BS of the t-th tier, and $\sum_{\substack{t\in\Phi_t\setminus t_0\\ t\in\{m,s\}}}\sqrt{P_t L_{t,k}}\mathbf{W}_{t,k}\mathbf{s}_t$ is the aggregate interference from MBS-tier and SBS-tier, the channel matrix $\mathbf{W}_{t,k}$ captures the overall channel effects, which encompass both direct paths and the signals reflected off the RIS. Also, $\boldsymbol{\Theta} = \frac{1}{\sqrt{\Lambda}}\boldsymbol{\Phi}$, $\mathbf{D}$ represents the precoding matrix of the tagged BS, $\mathbf{D}_t$ represents the precoding matrix from the other tier BS, and $\mathbf{n}_k$ is the zero mean additive white Gaussian noise (AWGN) vector at the UE$_k$ whose covariance matrix follows $\sigma_k^2\mathbf{I}_{U_r}$.

In general, a decision vector $\mathbf{u}_k$ is employed by the UE$_k$ to detect the received signal. The processed signal is written as

$$\mathbf{u}_k^{\mathrm{H}}\mathbf{y}_k = \sqrt{\Lambda L_{t_0,r,k}}\mathbf{u}_k^{\mathrm{H}}\mathbf{H}_k\boldsymbol{\Theta}_r\mathbf{G}_k\mathbf{D}\sqrt{P_t}\mathbf{s}_{t_0}(t) + \underbrace{\sum_{\substack{t\in\Phi_t\setminus t_0\\ t\in\{m,s\}}}\sqrt{P_t L_t}\mathbf{u}_k^{\mathrm{H}}\mathbf{W}_{t,k}\mathbf{D}_t\mathbf{s}_t}_{\text{interference from other BSs}} + \mathbf{u}_k^{\mathrm{H}}\mathbf{n}_k, \tag{6}$$

where $\mathbf{u}_k$ is a $U_r \times 1$ decision vector. Based on (6), the SINR at the user for the UE$_k$ to detect the signal of UE$_j$ is written in (15) and the SINR the user for the UE$_k$ to detect its own signal is written in (16). However, to establish a comprehensive framework for further analysis, we make the assumption that the active beamforming weights at the BS follow $\mathbf{D} = \mathbf{I}_{M_t}$ [63]. The precoding matrix of other tiers BS $\mathbf{D}_t$ can also be defined in a similar way. The identification vector for UE$_k$ can be represented as an $R \times 1$ vector filled with all ones, denoted as $\mathbf{u}_k^{\mathrm{H}} = [1 \cdots 1]$. Next, we follow the passive beamforming design of [59] to minimize the interference at the receivers and write the SINR equations at the user k. From [59] the channel gain of UE$_k$ is

$$\tilde{\mathbf{h}}_k = \begin{bmatrix} \sum_{r=1}^{R}|h_{1,r}||g_{r,n}| \\ \vdots \\ \sum_{r=1}^{R}|h_{U_r,r}||g_{r,n}| \end{bmatrix}. \tag{7}$$

The users' detection vectors are developed to i) reduce interference, and ii) function effectively under both RIS and non-RIS conditions. In the RIS situation, since the BS-user links are prohibited, the channel matrix of the user k can be translated to a $U_r \times M_t$ matrix, stated as

$$\hat{\mathbf{H}}_k = \mathbf{H}_k\boldsymbol{\Theta}\mathbf{G}. \tag{8}$$

Consequently, the subsequent condition needs to be satisfied:

$$\mathbf{u}_k^{\mathrm{H}}\hat{\mathbf{H}}_k\mathbf{d}_i = 0, \tag{9}$$

for any $i \neq k$. Because the active beamforming weights are components of an identity matrix, the aforementioned condition in (9) is converted as

$$\mathbf{u}_k^{\mathrm{H}}\hat{\mathbf{h}}_i = 0, \tag{10}$$

where $\hat{\mathbf{h}}_i$ represents the i-th column of matrix $\hat{\mathbf{H}}_k$ in (8). Hence, based on the zero-forcing design, the k-th column of $\hat{\mathbf{H}}_k$ can be eliminated. This leads to

$$\tilde{\mathbf{H}}_k = \left[\hat{\mathbf{h}}_1 \ldots \hat{\mathbf{h}}_{k-1}\hat{\mathbf{h}}_{k+1} \ldots \hat{\mathbf{h}}_{M_t}\right], \tag{11}$$

where $\tilde{\mathbf{H}}_k$ contains $U_r \times (M_t - 1)$ elements. Thus the condition in (9) is given as

$$\mathbf{u}_k^{\mathrm{H}}\tilde{\mathbf{H}}_k = 0. \tag{12}$$

Hence, we get the detection vector of the k-th user from the null space of $\tilde{\mathbf{H}}_k$, which is given as

$$\mathbf{u}_k = \mathbf{Q}_k \mathbf{z}_k, \tag{13}$$

where $\mathbf{Q}_k$ represents the left singular matrix of $\tilde{\mathbf{H}}_k$. Subsequently, we apply the traditional maximal ratio combining (MRC) technique, yielding $\mathbf{z}_k$ as follows

$$\mathbf{z}_k = \frac{\mathbf{Q}_k^{\mathrm{H}} \hat{\mathbf{h}}_k}{|\mathbf{Q}_k^{\mathrm{H}} \hat{\mathbf{h}}_k|}. \tag{14}$$

To guarantee the presence of the left singular vector in (11), the number of transmit antennas must be smaller than the number of receive antennas, i.e. $U_r \geq M_t$. In other cases, there is no feasible solution. Active beamformers with higher power and complexity can lower the need for several receive antennas. (15) provides the SINR of UE$_k$ to detect UE$_j$ applying the proposed active beamforming and detection vectors. Furthermore, the SINR of user k to detect its own signal is given in (16). It is observed that

$$|\mathbf{u}_k^{\mathrm{H}}|^2 = \left(\frac{|\mathbf{Q}_k \mathbf{Q}_k^{\mathrm{H}}|^2}{|\mathbf{Q}_k^{\mathrm{H}}|} \right)^2 = |\mathbf{Q}_k^{\mathrm{H}}|^2, \tag{17}$$

and

$$|\mathbf{u}_k^{\mathrm{H}} \mathbf{h}_k|^2 = \left(\frac{|\mathbf{Q}_k \mathbf{Q}_k^{\mathrm{H}} \mathbf{h}_k^2|^2}{|\mathbf{Q}_k^{\mathrm{H}}|} \right)^2 = |\mathbf{h}_k \mathbf{Q}_k^{\mathrm{H}}|^2. \tag{18}$$

Based on (7) and observing that $\mathbf{Q}_k^{\mathrm{H}} \mathbf{Q}_k = \mathbf{I}_T$ in (17) with $T = U_r - M_t + 1$, the UE$_k$ channel gain is given as [64]

$$\mathbf{h}_k = \begin{bmatrix} \sum_{r=1}^{R} |h_{1,r}||g_{r,n}| \\ \vdots \\ \sum_{r=1}^{R} |h_{T,r}||g_{r,n}| \end{bmatrix}. \tag{19}$$

Thus, the SINR expressions of (15) and (16) be rewritten as

$$\gamma_{k \to j} = \frac{\| \mathbf{h}_k \|^2 \, \Lambda L_{t_0,r,k} P_t a_j}{\| \mathbf{h}_k \|^2 \, \Lambda L_{t_0,r,k} P_t \sum_{i=j+1}^{K} a_i + \varepsilon P_t |h_I|^2 + \mathcal{I} + \| \mathbf{I}_T \|^2 \, \sigma_k^2}, \tag{20}$$

$$\gamma_{k \to k} = \frac{\| \mathbf{h}_k \|^2 \, \Lambda L_{t_0,r,k} P_t a_k}{\| \mathbf{h}_k \|^2 \, \Lambda L_{t_0,r,k} P_t \sum_{i=k+1}^{K} a_i + \hat{\varepsilon} P_t |\hat{h}_I|^2 + \mathcal{I} + \| \mathbf{I}_T \|^2 \, \sigma_k^2}, \tag{21}$$

where $\gamma_{k \to j} = SINR_{k \to j}$ and $\gamma_{k \to k} = SINR_{k \to k}$, $\mathcal{I} = \sum_{\substack{t \in \Phi_t \setminus t_0 \\ t \in \{m,s\}}} P_t L_{t,k} |\mathbf{u}_k^{\mathrm{H}} \mathbf{w}_k|^2$ and $\varepsilon{=}\hat{\varepsilon} = 1$ represents the imperfect SIC case such that $h_I = \hat{h}_I \sim \mathcal{CN}(0, \sigma_I^2)$. With careful design of the detection vector, the MIMO system can be reduced into a simple single-input single-output (SISO) case where the use of SIC yields the optimal performance [63]. It is to be noted that the BS needs to know the order of the users' effective channel gain to implement NOMA. However, the SIC may not be perfect, and a residual interference term exists due to imperfect SIC in the SINR expression.

The direct link BS-UE$_k$ are considered in the absence of RIS, and the small-scale fading matrix of these links follows the Rayleigh fading channel model, as depicted below

$$\mathbf{W}_k = \begin{bmatrix} w_{1,1} & \cdots & w_{1,M_t} \\ \vdots & \ldots & \vdots \\ w_{U_r,1} & \cdots & w_{U_r,M_t} \end{bmatrix} \tag{22}$$

where $\mathbf{W}_k$ is a $U_r \times M_t$ matrix. Again, by applying (9) to (21), the beamforming weights and detection vectors can be determined for non-RIS case. The user k channel gain for direct transmission is given as

$$\mathbf{w}_k = \begin{bmatrix} \sum_{t=1}^{M_t} |w_{1,t}| \\ \vdots \\ \sum_{r=1}^{M_t} |w_{T,t}| \end{bmatrix} \tag{23}$$

where $T = U_r - M_t + 1$. Thus, the SINR of user k for direct transmission case can be expressed as

$$\gamma_{k \to j} = \frac{\| \mathbf{w}_k \|^2 \, \Lambda L_{t_0,k} P_t a_j}{\| \mathbf{w}_k \|^2 \, \Lambda L_{t_0,k} P_t \sum_{i=j+1}^{K} a_i + \varepsilon P_t |h_I|^2 + \mathcal{I} + \| \mathbf{I}_T \|^2 \, \sigma_k^2} \tag{24}$$

$$\gamma_{k \to k} = \frac{\| \mathbf{w}_k \|^2 \, \Lambda L_{t_0,k} P_t a_k}{\| \mathbf{w}_k \|^2 \, \Lambda L_{t_0,k} P_t \sum_{i=k+1}^{K} a_i + \hat{\varepsilon} P_t |\hat{h}_I|^2 + \mathcal{I} + \| \mathbf{I}_T \|^2 \, \sigma_k^2}, \tag{25}$$

C. SINR at sensing channels

Since all prospective targets are in the BS's NLoS zones, there are no LoS links that can be used to do target sensing. However, the sensing can be performed by the RIS's reflection-LoS links. The sensing signal is defined as

$$\mathbf{x} = \mathbf{W}_r \mathbf{s}_r \tag{26}$$

where $\mathbf{s} \in \mathbb{C}^{M_t \times 1}$ represents the transmit symbol, $\mathbf{W}_r = [\mathbf{w}_{r,1}, \mathbf{w}_{r,2}, \cdot, \mathbf{w}_{r,M_t}]$ represents the beamforming matrices for target sensing. Pseudo-random coding is used to obtain the sensing signal, such that $\mathbb{E}[\mathbf{s}_r] = 0$ and $\mathbb{E}[\mathbf{s}_r \mathbf{s}_r^{\mathrm{H}}] = \mathbf{I}_{M_t}$ [65]. Thus, the sensing signal covariance matrix is written as

$$\mathbf{R} = \mathbb{E}[\mathbf{x}\mathbf{x}^{\mathrm{H}}] = \mathbf{W}_r \mathbf{W}_r^{\mathrm{H}} \tag{27}$$

The channel of BS-RIS link $\mathbf{H}_k$, is determined by the direction of arrival (DoA) of the RIS ψ_2 and the angles-of-departure (AoD) of the BS ψ_1, which is expressed as

$$\mathbf{H}_k = \mathbf{r}_2(\psi_2) \mathbf{r}_1^H(\psi_1) \tag{28}$$

Vectors $\mathbf{r}_1(\psi_1)$ and $\mathbf{r}_2(\psi_2)$ are, respectively, the array response vectors of the BS and the RIS. They are mathematically defined as

$$\mathbf{r}_1(\psi_1) = \left[1, e^{-j2\pi d_b \frac{\sin(\psi_1)}{\lambda}}, \ldots, e^{-j2\pi d_b (M_t - 1) \frac{\sin(\psi_1)}{\lambda}}\right]^T,$$
$$\mathbf{r}_2(\psi_2) = \left[1, e^{-j2\pi d_r \frac{\sin(\psi_2)}{\lambda}}, \ldots, e^{-j2\pi d_r (R-1) \frac{\sin(\psi_2)}{\lambda}}\right]^T, \tag{29}$$

$$\gamma_{k\to j}=\frac{\left|\mathbf{u}_k^{\mathrm{H}}\mathbf{h}_k\right|^2\Lambda L_{t_0,r,k}P_t a_j}{\left|\mathbf{u}_k^{\mathrm{H}}\mathbf{h}_k\right|^2\Lambda L_{t_0,r,k}P_t\sum\limits_{i=j+1}^{K}a_i+\sum\limits_{\substack{t\in\Phi_t\setminus t_0\\ t\in\{m,s\}}}P_tL_{t,k}|\mathbf{u}_k^{\mathrm{H}}\mathbf{w}_k|^2+|\mathbf{u}_k^{\mathrm{H}}|^2\sigma_k^2}. \tag{15}$$

$$\gamma_{k\to k}=\frac{\left|\mathbf{u}_k^{\mathrm{H}}\mathbf{h}_k\right|^2\Lambda L_{t_0,r,k}P_t a_k}{\left|\mathbf{u}_k^{\mathrm{H}}\mathbf{h}_k\right|^2\Lambda L_{t_0,r,k}P_t\sum\limits_{i=k+1}^{K}a_i+\sum\limits_{\substack{t\in\Phi_t\setminus t_0\\ t\in\{m,s\}}}P_tL_{t,k}|\mathbf{u}_k^{\mathrm{H}}\mathbf{w}_k|^2+|\mathbf{u}_k^{\mathrm{H}}|^2\sigma_k^2}. \tag{16}$$

where λ is carrier wavelength, d_b and d_r are the separation between the BS's antennas and the adjacent reflecting components of RIS, respectively. For analysis, we set $d_b = d_r = \frac{\lambda}{2}$. Considering the limited spatial extent of the target, the incident signal is solely reflected by the point target. Thus, the target response matrix between the RIS and the target can be denoted as $\mathcal{A} = \mathbf{r}_3(\psi_3)\mathbf{r}_3^{\mathrm{H}}(\psi_3) \in \mathbb{C}^{R\times R}$, where ψ_3 is the DoA w.r.t. the active RIS, and the steering vector $\mathbf{r}_3(\psi_3)$ is defined similarly as those in (29).

In sensing, the echo reflected back at the BS includes both thermal noise generated by the active RIS and the message transmitted over the target-RIS-BS link. Since the reflected echo from the BS-RIS-BS link does not contain any information about the target, it can be regarded as interference in target detection. Therefore, the received sensing signal at the BS can be depicted as

$$\begin{aligned}\mathbf{y}_b =&\mathbf{H}_k^h\mathbf{\Phi}^{\mathrm{H}}\mathcal{A}\mathbf{\Phi}\mathbf{H}\mathbf{x}+\mathbf{H}_k^h\Phi^{\mathrm{H}}\mathcal{A}\mathbf{\Phi}\mathbf{n}_1\\ &+\mathbf{H}_k^{\mathrm{H}}\mathbf{\Phi}\mathbf{n}_1+\mathbf{H}_k^{\mathrm{H}}\mathbf{\Phi}^{\mathrm{H}}\mathbf{n}_2+\eta\mathbf{H}_k^{\mathrm{H}}\mathbf{\Phi}\mathbf{H}_k\mathbf{x}+\mathbf{n}_t,\end{aligned} \tag{30}$$

where where $\eta \in [0,1]$ represents the ability to cancel self interference. $\eta = 0$ is for the case with perfect self-interference cancellation, whereas $\eta = 1$ indicates no interference cancellation. $\mathbf{n}_t$ represents AWGN at BS, which follows $\mathbf{n}_t \sim \mathcal{CN}(0, \sigma^2\mathbf{I}_{M_t})$ with the noise power of σ^2. Defining $\mathbf{B} \triangleq \mathbf{H}_k^{\mathrm{H}}\mathbf{\Phi}^{\mathrm{H}}\mathcal{A}\mathbf{\Phi}\mathbf{H}_k \in \mathbb{C}^{M_t\times M_t}$ and $\mathbf{C} \triangleq \mathbf{H}_k^{\mathrm{H}}\Phi^{\mathrm{H}}\mathcal{A}\Phi \in \mathbb{C}^{M_t\times R}$, the sensing SINR is written [51] as

$$\gamma_s = \mathrm{Tr}(\mathbf{BRB}^{\mathrm{H}}\mathbf{J}^{-1}). \tag{31}$$

The interference-plus-noise covariance matrix $\mathbf{J}$ is given by

$$\mathbf{J} = \mathbf{D} + \mathbf{ERE}^{\mathrm{H}}, \tag{32}$$

where $\mathbf{D} = \sigma^2(\mathbf{H}_k^{\mathrm{H}}\mathbf{\Phi}\mathbf{\Phi}^{\mathrm{H}}\mathcal{A}\mathbf{H}_k+\mathbf{H}_k^{\mathrm{H}}\mathbf{\Phi}^{\mathrm{H}}\mathcal{A}\mathbf{\Phi}\mathbf{\Phi}^{\mathrm{H}}\mathbf{H}_k)+\sigma^2\mathbf{C}\mathbf{C}^{\mathrm{H}}+2\sigma^2\mathbf{H}^{\mathrm{H}}\mathbf{\Phi}^{\mathrm{H}}\mathbf{\Phi}\mathbf{H}+\sigma^2\mathbf{I}_{M_t}$ is the equivalent noise covariance matrix and $\mathbf{E} = \eta\mathbf{H}_k^{\mathrm{H}}\mathbf{\Phi}\mathbf{H}_k$.

D. Association Criteria

The nearest association criterion [66] for the typical UE$_k$ is considered in this section. In particular, the typical UE$_k$ connects to its closest BS for a direct transmission case, and the typical user chooses the nearest RIS when there is a blockage between UE$_k$ and the tagged BS. The probability density function (PDF) of the distances is written as

$$f_{t,k}(r) = 2\pi\lambda_t r\exp(-\pi\lambda_t r^2), \tag{33}$$

and

$$f_{r,k}(r) = 2\pi\lambda_R r\exp(-\pi\lambda_R r^2), \tag{34}$$

where λ_t is the density of BS of t-th tier and λ_R is the density of RIS. The RIS is considered to be at a known location from the BSs across all tiers.

III. Performance Analysis

Lemma 1: *Assuming that the elements in $\boldsymbol{G}_k$ and $\boldsymbol{H}_k$ are i.i.d. with $m_1 \neq m_2$ respectively, and that the R RIS elements simultaneously serve K users with $R \geq U_r \geq M_t$. The PDF of the effective channel gain at UE$_k$ in the high-SNR regime is given by*

$$f_{|h_k|^2}(x) = \frac{m^R}{2m_iR}x^{2m_iR-1}e^{-2\sqrt{m_im_x}x}, \tag{35}$$

where m_i=$\min\{m_1,m_2\}$, m_x=$\max\{m_1,m_2\}$, and m=$\frac{\sqrt{\pi}4^{m_i-m_x+1}(m_im_x)^{m_i}\Gamma(2m_i)\Gamma(2m_x-2m_i)}{\Gamma(m_i\Gamma(m_x)\Gamma(m_i+m_x+0.5)}$. The cumulative distribution function (CDF) of the effective channel gain can be expressed as

$$F_{|h_k|^2}(x) = \frac{m^R\left(4m_im_x\right)^{-m_iR}}{\Gamma(2m_iR)}\gamma\left(2m_iR, 2\sqrt{m_im_x}x\right). \tag{36}$$

Proof: Please see Appendix A.

A. Outage Probability of blocked user

The SIC is implemented at the k-th user. This entails decoding and removing the information pertaining to the j-th user such that $(k \geq j \geq 1)$ before proceeding to detect its own signal. An outage event is indicated when the k-th user fails to detect the j-th user, denoted by

$$\mathcal{E}_{k\to j} = \left\{\gamma_{k\to j} < \gamma_{th_k}\right\} \tag{37}$$

where $\gamma_{th_k} = 2^{R_{k,j}} - 1$ with $R_{k,j}$ being the target data rate at the k-th user. The outage probability of the k-th user for RIS-NOMA networks is provided in the subsequent theorem.

Theorem 2: *The outage probability of the UE$_k$ under the composite fading for the RIS-assisted MIMO-NOMA HetNet is given by*

$$P_{out}^{k} = \frac{\pi^2 \lambda_R m^R (4m_i m_x)^{-m_i R}}{N\Gamma(2m_i R)} \int_0^{\infty} \sum_{n=1}^{N} \sqrt{1-\phi_i^2} \frac{(\phi_i+1)\mathcal{Y}_t}{2} \times \gamma\left(2m_i R, 2\sqrt{m_i m_x} \frac{\Upsilon_k^*(\mathcal{I}+1)}{T\Lambda(r_{t,r})^{-\alpha}} \left(\frac{(\phi_i+1)\mathcal{Y}_t}{2}\right)^{\alpha}\right) \times \exp\left(-\pi\lambda_R \left(\frac{(\phi_i+1)\mathcal{Y}_t}{2}\right)^2\right) \frac{w^{m_I-1}e^{-m_I w}}{\Gamma(m_I)} dw \tag{38}$$

where $\phi_i = \cos\left(\frac{2i-1}{2N}\right)$, and N is the complex accuracy trade-off parameter for the G-C quadrature [67].

Proof: Please see Appendix B.

B. Outage probability of user with direct transmission

Now, we will evaluate the outage probability for the scenario where UE$_k$ receives signal directly from the BS.

Theorem 3: *The outage probability of the UE$_k$ under Rician fading for the RIS-NOMA HetNet which receives the signal only from the nearest BS is given by*

$$\hat{P}_{out}^{k} \approx \frac{\pi^2 \mathcal{Y}_s^2 \lambda_t}{2N\Gamma(T)} \int_0^{\infty} \sum_{n=1}^{N} \sqrt{1-\phi_i^2}(\phi_i+1) \times \gamma\left(T, \frac{\Upsilon_k^*(\mathcal{I}+1)}{T\Lambda}\left(\frac{(\phi_i+1)\mathcal{Y}_t}{2}\right)^{\alpha}\right) \times \exp\left(-\pi\lambda_R \left(\frac{(\phi_i+1)\mathcal{Y}_t}{2}\right)^2\right) \frac{w^{m_I-1}e^{-m_I w}}{\Gamma(m_I)} dw. \tag{39}$$

Proof: Please see Appendix C.

C. Diversity Order

The diversity order is evaluated to improve comprehension to distinguish the outage patterns in RIS-NOMA enabled HetNet. This performance metric has the potential to demonstrate the rate at which the likelihood of an outage reduces with the SNR [68]. Stated differently, a higher diversity order denotes a faster decaying rate of decrease in the likelihood of an outage and a stronger resistance to fading. The diversity order is described as:

$$\mathcal{D} = -\lim_{\rho\to\infty} \frac{\log P_{out,asym}^{k}}{\log \rho}, \tag{40}$$

where $P_{out,asym}^{k}$ denotes the asymptotic outage probability when $\rho \to \infty$. Initially, we obtain an estimated asymptotic outage probability for the scenario where a UE$_k$ is served by the BS and the RIS, leading to its association with the nearest BS. The asymptotic outage probability for UE$_k$ is presented in the subsequent corollary.

Corollary 1: The asymptotic outage probability for the scenario where the link between UE$_k$ and BS is blocked and UE$_k$ is served by the RIS, leading to its association with the nearest RIS. The outage probability of UE$_k$ for this scenario is

$$P_{out}^{k} = \frac{\pi^2 \lambda_R m^R (4m_i m_x)^{-m_i R}}{N\Gamma(2m_i R)} \sum_{n=1}^{N} \sqrt{1-\phi_i^2} \frac{(\phi_i+1)\mathcal{Y}_t}{2} \times \left(2\sqrt{m_i m_x} \frac{\Upsilon_k^*(\mathcal{I}+1)}{T\Lambda(r_{t,r})^{-\alpha}} \left(\frac{(\phi_i+1)\mathcal{Y}_t}{2}\right)^{\alpha}\right)^{2m_i R} \times \sum_{s=0}^{\infty} -\left(\frac{2\sqrt{m_i m_x}}{s!(2m_i R+s)} \frac{\Upsilon_k^*(\mathcal{I}+1)}{T\Lambda(r_{t,r})^{-\alpha}} \left(\frac{(\phi_i+1)\mathcal{Y}_t}{2}\right)^{\alpha}\right)^{s} \times \exp\left(-\pi\lambda_R \left(\frac{(\phi_i+1)\mathcal{Y}_t}{2}\right)^2\right) \tag{41}$$

Proof: Please see Appendix D.

Remark 1: By substituting (41) *into* (40)*, $\mathcal{D} = 2m_i R$, which depends upon quantity of RIS elements R and the dominant LoS link between BS-RIS and RIS-UE$_k$.*

Corollary 2: The asymptotic outage probability for the direct transmission scenario between UE$_k$ and BS is evaluated following similar steps as used in (41)*, the asymptotic outage probability of UE$_k$ for this scenario is given as*

$$\hat{P}_{out}^{k} \approx \frac{\pi^2 \mathcal{Y}_s^2 \lambda_t}{2N\Gamma(T)} \sum_{n=1}^{N} \sqrt{1-\phi_i^2}(\phi_i+1) \times \left(\frac{\Upsilon_k^*(\mathcal{I}+1)}{T\Lambda}\left(\frac{(\phi_i+1)\mathcal{Y}_t}{2}\right)^{\alpha}\right)^{T} \times \sum_{s=0}^{\infty} -\left(\frac{\Upsilon_k^*(\mathcal{I}+1)}{s!(2m_i R+s)}\left(\frac{(\phi_i+1)\mathcal{Y}_t}{2}\right)^{\alpha}\right)^{s} \times \exp\left(-\pi\lambda_R \left(\frac{(\phi_i+1)\mathcal{Y}_t}{2}\right)^2\right). \tag{42}$$

Remark 2: By substituting (42) *into* (40)*, $\mathcal{D} = T$, aligning with the number of independent channels exists between the BS and UE$_k$.*

D. Delay Limited (DL) System Throughput

In the scenarios involving DL transmission, the system throughput is determined by calculating the outage probability at a fixed rate, denoted by R_i. Consequently, the throughput of the DL system in RIS-NOMA-assisted HetNet over Rician fading channels is described as

$$T_{sys} = \sum_{i=1}^{K} (1 - P_{out}^{i}) R_i, \tag{43}$$

where P_{out}^{i} is the outage probability at the i^{th} NOMA user.

IV. Ergodic Rate

This section describes the ergodic rate of a UE$_k$ for RIS-NOMA networks on the assumption that a typical user can accurately determine user information by using the SIC method. The ergodic rate of UE$_k$ is described as

$$E_{rg}^{k} = \mathbb{E}\left[\log\left(1 + SINR_{k\to k}\right)\right]. \tag{44}$$

$$E_{rg}^{k}=\frac{1}{\ln 2}\int_{0}^{\infty}\frac{1}{(1+x)}\left(1-\frac{\pi^{2}\lambda_{R}m^{R}\left(4m_{i}m_{x}\right)^{-m_{i}R}}{N\Gamma(2m_{i}R)}\int_{0}^{\infty}\sum_{n=1}^{N}\gamma\left(2m_{i}R,2\sqrt{m_{i}m_{x}}\frac{\Upsilon_{k}^{*}(\mathcal{I}+\hat{\varepsilon}P_{t}w+1)}{T\Lambda(r_{t,r})^{-\alpha}}\left(\frac{(\phi_{i}+1)\mathcal{Y}_{t}}{2}\right)^{\alpha}\right)\right.$$
$$\left.\times\sqrt{1-\phi_{i}^{2}}\frac{(\phi_{i}+1)\mathcal{Y}_{t}}{2}\exp\left(-\pi\lambda_{R}\left(\frac{(\phi_{i}+1)\mathcal{Y}_{t}}{2}\right)^{2}\right)\frac{w^{m_{I}-1}e^{-m_{I}w}}{\Gamma(m_{I})}dw\right)dx. \tag{45}$$

Theorem 4: *The ergodic rate of blocked user UE$_k$ served via active RIS in a MIMO HetNet is given by* (45) *as shown on the top of the next page.*

Proof: Substituting the expression of $\gamma_{k\to k}$ from (21) after considering $X=|h_k|^2$ we get

$$E_{rg}^{k}=\mathbb{E}\Bigg[\log\left(1+\underbrace{\frac{X\Lambda L_{t_0,r,k}P_{t}a_{k}}{X\Lambda L_{t_0,r,k}P_{t}\sum_{i=k+1}^{K}a_{i}+\mathcal{I}+\hat{\varepsilon}P_{t}|\hat{h}_{I}|^{2}+\parallel\mathbf{I}_{T}\parallel^{2}\sigma_{k}^{2}}}_{\mathrm{X}_2}\right)\Bigg]$$
$$=\frac{1}{\ln 2}\int_{0}^{\infty}\frac{1-F_{X_2}(x)}{1+x}dx. \tag{46}$$

Substituting the CDF of $F_{X_2}(x)$, which is nothing but the outage probability evaluated at $\gamma_{th}=x$, from (B.3) and substituting the PDF of $|\hat{h}_I|^2$. The ergodic rate is expressed in (47) as shown on the top of the next page. □

Theorem 5: *The ergodic rate for the scenario where the BS serves UE$_k$ in a HetNet directly is given by* (47)*.*

Proof: Substituting the expression of $\gamma_{k\to k}$ from (25) after considering $X=|w_k|^2$ we get

$$E_{rg}^{k}=\mathbb{E}\Bigg[\log\left(1+\underbrace{\frac{X\Lambda L_{t_0,k}P_{t}a_{k}}{X\Lambda L_{t_0,k}P_{t}\sum_{i=k+1}^{K}a_{i}+\mathcal{I}+\hat{\varepsilon}P_{t}|\hat{h}_{I}|^{2}+\parallel\mathbf{I}_{T}\parallel^{2}\sigma_{k}^{2}}}_{\mathrm{X}_3}\right)\Bigg]$$
$$=\frac{1}{\ln 2}\int_{0}^{\infty}\frac{1-F_{X_3}(x)}{1+x}dx \tag{48}$$

Substituting the CDF of $F_{X_3}(x)$, which is nothing but the outage probability evaluated at $\gamma_{th}=x$, from (C.4) and substituting the PDF of $|\hat{h}_I|^2$. The ergodic rate is expressed in (45). □

V. Beampattern Analysis

The beampattern gain from the active RIS towards angle ψ is defined as

$$\mathcal{B}(\psi)\triangleq\mathbb{E}\left(|\mathbf{r}_{3}^{\mathrm{H}}(\psi)\mathbf{\Phi}\mathbf{H}_{k}\mathbf{x}|^{2}\right)$$
$$=\mathbf{r}_{3}^{\mathrm{H}}(\psi)\mathbf{\Phi}\mathbf{H}\mathbf{R}\mathbf{H}_{k}^{\mathrm{H}}\mathbf{\Phi}^{\mathrm{H}}\mathbf{r}_{3}(\psi). \tag{49}$$

TABLE I: SIMULATION PARAMETERS

Parameters	**Symbols**	**Value**
BS transmission power	P_t	40 W [69]
BS density, RIS density, UE density	λ_t, λ_R, λ_u	$2km^{-2}$, $10km^{-2}$, $20km^{-2}$ [70]
Power allocation coefficients for NOMA	a_k	$0.7, 0.3$ [70]
Coverage radius of BS	R_m	1000 m [6]
Path loss exponent	α_t	4 [71]
Distance between BS and RIS	$r_{t_0,r}$	50m [65]
Target data rate	R_{cc}, R_{ce}	0.5 bps, 0.5 bps
Complexity accuracy parameter	N, L	10 [69], [71]
Noise power	σ_k^2, σ_t^2	-174+10log(BW) [72]
Bandwidth	BW	1000MHz [72]
RIS amplification coefficient	Λ	5 [72]
Transmit and Receive BS antennas	M_t and N_r	2 and 2 [59]
Receive user antennas	U_r	3 [59]

VI. Results and Discussions

This section showcases numerical findings derived from our investigation into the performance of the proposed MIMO-RIS HetNet we proposed. Monte Carlo simulations validate the precision of our analytical findings. For simulations, without the loss of generality, we consider the number of UE$_k$ as $K=2$. One of the blocked UEs is assumed to be served directly by the BS at the t-th tier and is known as the cell-edge user (CEU). The other blocked user is served with the help of RIS and is termed as the cell-edge user (CCU).

A. Outage Probability

Fig. 2 plots the outage probability of NOMA HetNets versus the SNR with setting to be $m_1=2$, $m_2=1$, $m_I=1$, for different number of RIS elements R. The target rates for the CCU and CEU are $R_{cc}=0.5$ and $R_{ce}=0.5$ BPCU, respectively. (38) and (39) are used for plotting the outage probability for CCU and CEU, respectively. The corresponding power allocation coefficients are $a_1=0.7$ and $a_2=0.3$ for the CEU and the CCU, respectively. The path loss factor $\alpha=4$. The curves obtained through numerical simulations closely align with the expressions obtained in the preceding sections. Increasing the number of RIS elements improves channel gain, resulting in an improved outage probability. The red and blue curves, and the results of equation (41) and (42) indicate that as the number of RIS elements increases from $R=1,2$, and 3 the diversity order improved to $2, 4$, and 6, respectively. This indicates that increasing the number of RIS elements reduces

$$E_{rg}^{k} = \frac{1}{\ln 2}\int_{0}^{\infty}\frac{1}{(1+x)}\left(1-\frac{\pi^2\mathcal{Y}_s^2\lambda_t}{2N\Gamma(T)}\int_{0}^{\infty}\sum_{n=1}^{N}\sqrt{1-\phi_i^2}(\phi_i+1)\gamma\left(T,\frac{\Upsilon_k^*(\mathcal{I}+\hat{\varepsilon}P_t w+1)}{T\Lambda}\left(\frac{(\phi_i+1)\mathcal{Y}_t}{2}\right)^{\alpha}\right)\times \right.$$
$$\left.\exp\left(-\pi\lambda_R\left(\frac{(\phi_i+1)\mathcal{Y}_t}{2}\right)^2\right)\frac{w^{m_I-1}e^{-m_I w}}{\Gamma(m_I)}dw\right)dx. \tag{47}$$

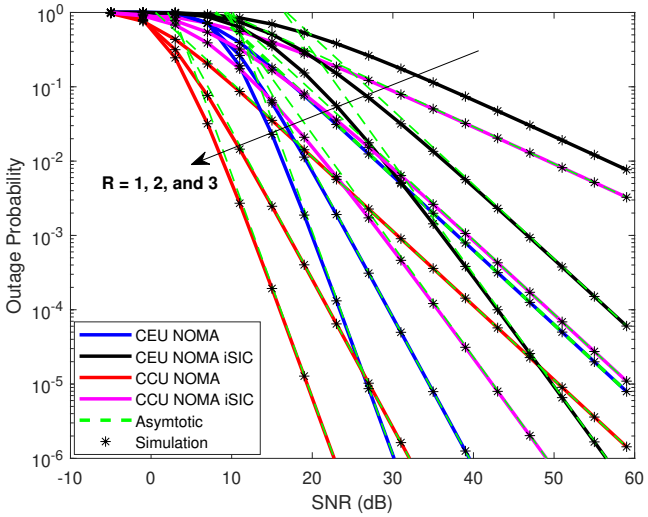

Fig. 2: Outage probability of users with transmit SNR.

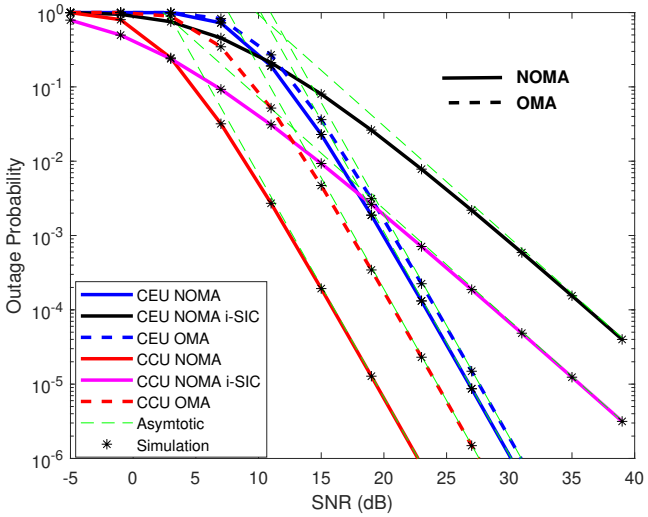

Fig. 3: Outage probability of users with transmit SNR.

the outage probability because the increased diversity order improves the channel. The inclination of the curves increases with the addition of RIS elements, supporting *Remark 1* and *Remark 2*. The dashed green curves represent the asymptotic results. There is a significant gap between the asymptotic and analytical results because the asymptotic results are derived at high SNR. However, in the high-SNR regime, there is a close agreement between the asymptotic and analytical results. Furthermore, the proposed system with i-SIC achieves a higher

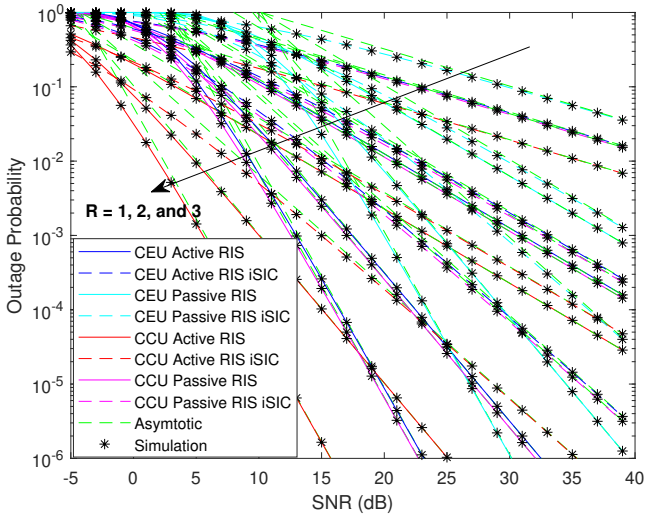

Fig. 4: Active RIS versus passive RIS comparison in terms of outage probability of users with transmit SNR.

outage probability than the perfect SIC case. This is due to the residual interference from i-SIC, which degrades the SINR.

Fig. 3 plots the outage probability of MIMO HetNets versus the SNR. The solid lines represent the outage probability of MIMO NOMA HetNet, and the dotted curves are for MIMO OMA. In the case of MIMO OMA, the transmission is divided into two equal phases. One is for the transmission to CCU, and the other is for the transmission to the CEU. The power is equally allocated to the CCU and the CEU for MIMO OMA. Notably, the outage performance of users employing NOMA surpasses that of RIS-OMA. This performance gain is due to NOMA's ability to enhance fairness when serving multiple users simultaneously compared to OMA. The outage characteristics of the CCU are better than those of the CEU in RIS-NOMA networks. This results from the evidence that the CCU achieves an improved diversity order than the CEU. Furthermore, i-SIC increases the outage probability compared to the ideal case due to residual interference and signal distortions affecting the overall system performance.

In Fig. 4, the outage probability of MIMO RIS HetNets is depicted by considering both active as well as passive RIS. Blue and red colours displayed the outage probability for the CEU and CCU for active RIS scenarios. Cyan and magenta colours displayed the outage probability for the CEU and CCU for the passive RIS scenario. The green dashes show the asymptotic outage probability expressions from (41) and (42). The outage performance of active RIS-NOMA surpasses

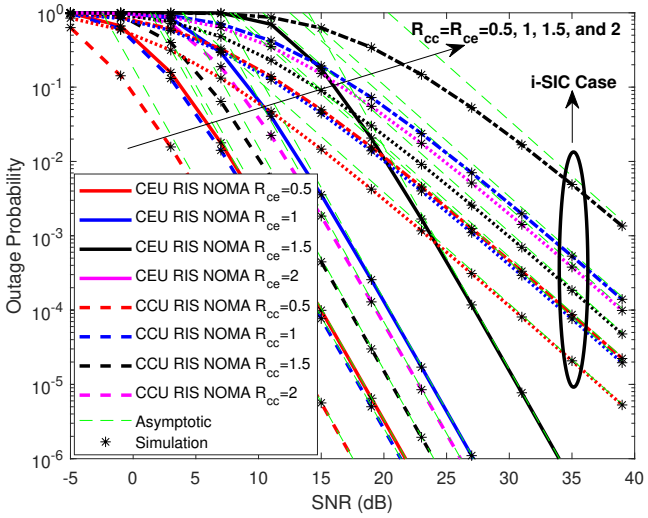

Fig. 5: Outage probability of users with transmit SNR for different values of target rates.

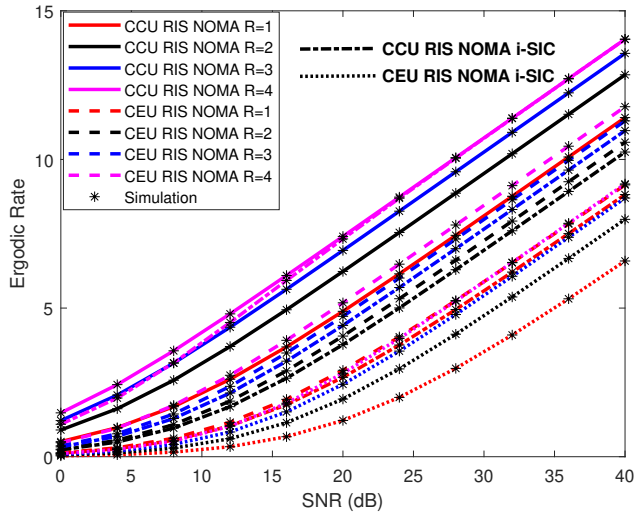

Fig. 6: Ergodic Rate of users with transmit SNR.

that of passive RIS-NOMA due to its enhanced reflection gain. Active RIS serves to amplify signals reflected back to users despite introducing amplified noise. The asymptotic curves closely match with the analytical expressions at high transmit SNR.

Fig. 5 illustrates the outage probability of RIS-NOMA networks across various SNR values, considering different target rates. A notable observation is that increasing target rates lead to higher outage probabilities in RIS-NOMA networks. This outcome is attributed to the direct correlation between achievable rates and target SNRs. It is shown that decoding the superposed signals becomes more advantageous for user pairings with smaller target SNRs. This proves to be beneficial for pairing users with weaker signal conditions in RIS-NOMA networks.

B. Ergodic Rate

In Fig. 6, the ergodic rates are graphed against SNR. The solid lines represent the ergodic rates of CCU in RIS-NOMA networks, while the dashed curves depict CEU rates for RIS-NOMA HetNets. These curves are generated using (45) and (47), respectively. The ergodic rate of UE_k served by both the BS and RIS is obtained using simulation. Furthermore, it is evident that, the CCU exhibit higher ergodic rates compared to the CEU. As the number of RIS elements R increases, the gap between the ergodic rate becomes smaller. Therefore, it is essential to consider the trade-off between the quantity of reflection elements in active RIS and the ergodic performance.

C. System Throughput

The system throughput for RIS-NOMA networks operating in the DL transmission is shown versus transmit SNR in Fig. 7, with $R_{cc} = 1.5, R_{ce} = 1$ BPCU. The curves are depicted based on equation (43). The figure reveals that, at high SNRs, the system throughput of RIS-NOMA surpasses

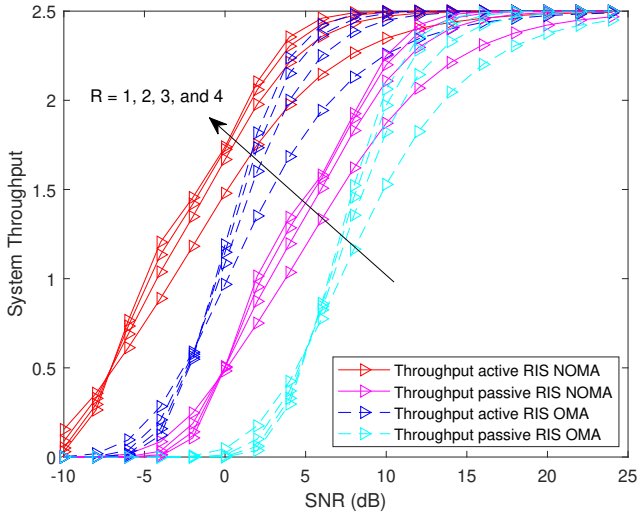

Fig. 7: System Throughput with transmit SNR for different values of RIS elements R.

that of RIS-OMA. This superiority is attributed to the effect of outage probability on the system throughput. As the quantity of reflection elements increases, RIS-NOMA networks are shown to be equipped with the ability to provide enhanced throughput. This fact can be rationalized by the better outage performance achieved for both the CCU and the CEU. Furthermore, the quantity of RIS elements improves the spectral efficiency. However, the improvement gradually decreases, which is also evident from the ergodic rate, as discussed previously. Furthermore, the active RIS attain throughput rates faster than passive RIS systems for both NOMA and OMA cases.

D. Received Sensing SINR at the BS

Based on (31) the received Sensing SINR vesus transmit SNR Fig. 8 is obtained. For simulation the number of RIS

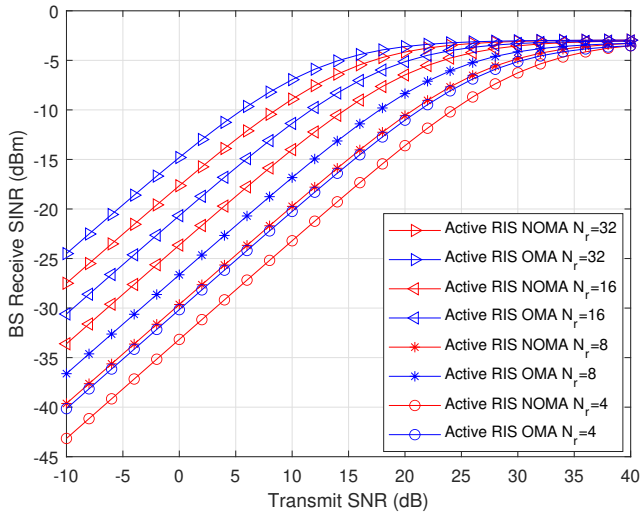

Fig. 8: BS received SINR versus BS transmit SNR.

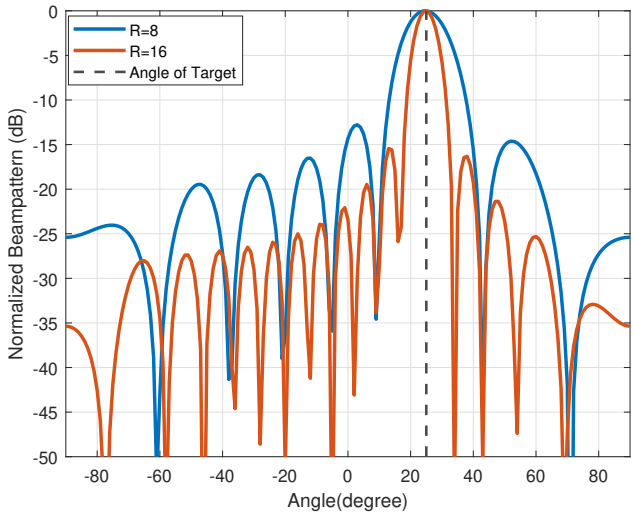

Fig. 9: Comparing the normalized sensor beampattern for varying reflecting element R.

elements are considered as R=16 and the channel is considered as serial independent concatenated channels. The received sensing SINR versus transmit SNR is a fundamental metric for evaluating the performance of a sensing system. Fig. 8 depicts the relationship between the transmit SNR and the received sensing SINR at the BS for different antennas. As the transmit SNR increases, the received sensing SINR also increases, indicating better detection performance, which is expected as more power leads to better signal quality. At low SNRs, the received SINR for NOMA is significantly lower than OMA, indicating a strong influence of interference. As SNR increases, the gap between NOMA and OMA narrows, however OMA consistently outperforms NOMA. For applications requiring high SINR, OMA is preferable, especially when high numbers of transmit antennas are feasible. NOMA can still be effective, however requires advanced interference management techniques to approach OMA performance levels. Despite the lower SINR observed in NOMA for sensing, NOMA offers better communication performance than OMA due to its ability to serve multiple users simultaneously with the same frequency-time resources. This makes NOMA suitable for communication-centric ISAC systems, where the primary focus is maximizing communication throughput while maintaining adequate sensing capabilities. OMA is preferable for applications requiring high SINR, especially when high numbers of transmit antennas are feasible. The lower interference in OMA systems makes them suitable for scenarios where precise target sensing is critical. Furthermore, as the number of antennas increases, the system can achieve high SINR at lower transmit SNR levels. This means that for systems with a large number of antennas, it is possible to maintain high performance without the need for high transmit power, leading to energy-efficient designs.

E. Beampattern

For the beampattern, it is assumed that the channels are acknowledged and operate independently at both the BS and the RIS, we designate the angle from the BS to the RIS as 0°, and the target is assumed to be present between 10° to 30° from RIS. As seen in Fig. 9, increasing the quantity of reflecting elements in the active RIS can improve performance and lead to a smaller beam. However, this can result in greater performance deterioration when the angle between the active RIS and the target is incorrectly estimated, especially in high-mobility scenarios.

VII. Conclusion

The manuscript comprehensively explored the novel application of ISAC in active RIS-assisted NOMA-enabled MIMO HetNets. The analytical system model has considered independent homogeneous PPP for BSs, active RISs and UEs as IoT nodes, which provides a robust foundation for the evaluation of performance metrics in the downlink transmissions. The BS supports simultaneous target S&C. The work derives approximate expressions for the outage probability, ergodic rates and system throughput for two distinct scenarios. One involves the direct transmission from the BS to the typical blocked user, and the other entails transmission via active RIS. The practical case of i-SIC is considered at the receiver, thereby making the proposed system model more realistic. The numerical results demonstrate the efficacy of RIS-NOMA, particularly when compared to RIS-OMA and conventional communication systems. The study revealed that RIS-NOMA outperforms RIS-OMA. Moreover, the dependence of outage performance on the number of RIS elements is also highlighted. The analysis of the ergodic rate confirmed the superiority of RIS-NOMA over RIS-OMA. The assessment of system throughput in delay-limited mode further solidified the advantages of RIS-NOMA, showcasing its higher throughput compared to RIS-OMA. The ergodic rates and system throughput increase with transmit SNR, gradually saturating due to increased self-interference and multi-tier interference. The sensing performance of RIS-NOMA in HetNets is char-

acterized by calculating the beampatern in the direction of the target.

APPENDIX A: PROOF OF LEMMA 1

With the elements of $|\mathbf{H}_k|$ and $|\mathbf{G}_k|$ being independent and identically distributed (i.i.d.), as described in [73], the PDF of the product of two Nakagami-m random variables is expressed as

$$f_{|h_k|^2}(x) = \frac{4\left(m_i m_x\right)^{\frac{m_i+m_x}{2}}}{\Gamma(m_i)\Gamma(m_x)} x^{m_i+m_x-1} I_{m_i-m_x}\left(2\sqrt{m_i m_l}x\right), \tag{A.1}$$

where $I_{m_i-m_x}(\cdot)$ represents the modified Bessel function of the second kind. Due to the complexity in calculating the modified Bessel function of the second kind in (A.1), we employ the Laplace transform of the PDF, which is expressed as:

$$\mathcal{L}_{|h_k|^2}(s) = \mathbb{E}\left(e^{-s\|h_k\|^2}\right) = \frac{4\left(m_i m_x\right)}{\Gamma(m_i)\Gamma(m_x)} \times \int_0^\infty x^{m_i+m_x-1} e^{-sx} I_{t_s-t_l}\left(2\sqrt{m_i m_x}x\right) dx. \tag{A.2}$$

With the help of [74, eq. (6.621.3)], (A.2) is rewritten as

$$\mathcal{L}_{|h_k|^2}(s) = m\left(s+2\sqrt{m_i m_x}\right)^{-2m_i} \times F\left(2m_i, m_i-m_x+\frac{1}{2}; m_i+m_x+\frac{1}{2}; \frac{s-2\sqrt{m_i m_x}}{s+2\sqrt{m_i m_x}}\right), \tag{A.3}$$

where $m = \frac{\sqrt{\pi}4^{m_i-m_x+1}(m_i m_x)^{m_i}\Gamma(2m_i)\Gamma(2m_x-2m_i)}{\Gamma(m_i\Gamma(m_x)\Gamma(m_i+m_x+0.5)}$, and $F(\cdot,\cdot;\cdot;\cdot)$ represents hypergeometric series. We focus on the high-SNR analysis, where $s \to \infty$. Then, upon assuming $m_1 \neq m_2$, the Laplace transform is approximated as

$$\mathcal{L}_{|h_k|^2}(s) \approx m\left(s+2\sqrt{m_i m_x}\right)^{-2m_i}. \tag{A.4}$$

Since the reflected signals are i.i.d., the overall effective channel gain can be given by

$$\mathcal{L}_{|h_k|^2}(s) \approx m^R\left(s+2\sqrt{m_i m_x}\right)^{-2m_i R}. \tag{A.5}$$

Utilizing the inverse Laplace transform for (A.5), we can derive the PDF and CDF in the high-SNR regime, as presented in (35) and (36), respectively, thereby concluding the proof.

APPENDIX B: PROOF OF THEOREM 1

From (37), the outage probability is rewritten as

$$P_{out}^k = \Pr[\min(\mathcal{E}_{k\to1}, \mathcal{E}_{k\to2}, \ldots, \mathcal{E}_{k\to k})]. \tag{B.1}$$

Then (B.1) be can rewritten as

$$P_{out}^k = \Pr\left[X < \frac{\Upsilon_k^*}{T\Lambda L_{t,r,k}}\left(\mathcal{I} + \varepsilon\rho_t \underbrace{|h_I|^2}_{\mathrm{w}} + 1\right)\right], \tag{B.2}$$

where $X = \frac{|h_k|^2}{\gamma_{th_k}}$, $\Upsilon_k^* = \max\{\Upsilon_1, \ldots, \Upsilon_k\}$, $\Upsilon_k = \frac{\gamma_{th_k}}{\rho_t(a_k - \gamma_{th_k}\sum_{i=k+1}^{M_t} a_i)}$ such that $a_m > \gamma_{th_k}$. Substituting for X from (36) and the distance distribution from (34), the outage probability is given by

$$P_{out}^k = \frac{2\pi\lambda_R m^R\left(4m_i m_x\right)^{-m_i R}}{\Gamma(2m_i R)} \times \int_0^\infty \int_0^{\mathcal{Y}_t} \gamma\left(2m_i R, 2\sqrt{m_i m_x}\frac{\Upsilon_k^*(\mathcal{I}+\varepsilon\rho_t w+1)}{T\Lambda(r_{t,r}r)^{-\alpha}}\right) \times r\exp(-\pi\lambda_R r^2) f_W(w) dz dr \tag{B.3}$$

Substituting the PDF of the random variable W as Gamma distributed with parameters $(m_I,\ m_I)$. In the computation of the definite integral in the above equation, we utilize the Gauss-Chebyshev (G-C) quadrature to approximate this specific type of integral [75]. The result is approximated as in (38).

APPENDIX C: PROOF OF THEOREM 2

From (24), the outage probability is rewritten as

$$P_{out}^k = \Pr\left[X < \frac{\Upsilon_k^*}{T\Lambda L_{t,k}}\left(\mathcal{I} + \varepsilon\rho_t w + 1\right)\right], \tag{C.1}$$

where $X = |w_k|^2$. The random variable X follows the chi-square distribution, and thus the PDF is given by

$$f_X(x) = \frac{e^{-x}}{(U_r - M_t)!} x^{U_r - M_t}. \tag{C.2}$$

Its CDF is given by

$$F_X(x) = \frac{\gamma(U_r - M_t + 1, x)}{(U_r - M_t)!} = \frac{\gamma(T, x)}{\Gamma(T)}, \tag{C.3}$$

where $T = U_r - M_t + 1$. Substituting the PDF of the random variable W as Gamma distributed with parameters (m_I, m_I), substituting (C.3) and the PDF of the BS association probability from (33) in (C.1), the outage probability is given by

$$P_{out}^k = \int_0^\infty \int_0^{\mathcal{Y}_t} \gamma\left(T, \frac{\Upsilon_k^*(\mathcal{I}+\varepsilon\rho_t w+1)}{T\Lambda(r)^{-\alpha}}\right) 2\pi\lambda_t r \times \exp(-\pi\lambda_t r^2)\frac{w^{m_I-1}e^{-m_I w}}{\Gamma(m_I)} dw dr. \tag{C.4}$$

We utilise the G-C quadrature to approximate the definite integral in the above equation. The result is presented in (39).

APPENDIX D: PROOF OF COROLLARY 1

To obtain the diversity of the system, we expand the lower incomplete gamma function substituting from [74, eq.(8.352.2)] into (38). The expression is shown in (D.1). Substituting the exponent term by its power series expansion, the outage probability can be written as in (41).

$$\gamma\left(2m_iR, 2\sqrt{m_im_x}\frac{\Upsilon_k^*(\mathcal{I}+1)}{T\Lambda(r_{t,r})^{-\alpha}}\left(\frac{(\phi_i+1)\mathcal{Y}_t}{2}\right)^{\alpha}\right) = \sum_{s=0}^{\infty}\frac{\Gamma[2m_iR]}{\Gamma[2m_im_x+s+1]}\left(\frac{2\sqrt{m_im_x}\Upsilon_k^*(\mathcal{I}+1)}{T\Lambda(r_{t,r})^{-\alpha}}\left(\frac{(\phi_i+1)\mathcal{Y}_t}{2}\right)^{\alpha}\right)^{2m_iR+s} \times \exp\left(-\left(2\sqrt{m_im_x}\frac{\Upsilon_k^*(\mathcal{I}+1)}{T\Lambda(r_{t,r})^{-\alpha}}\left(\frac{(\phi_i+1)\mathcal{Y}_t}{2}\right)^{\alpha}\right)\right), \quad \text{(D.1)}$$

REFERENCES

[1] D. C. Nguyen, M. Ding, P. N. Pathirana, A. Seneviratne, J. Li, D. Niyato, O. Dobre, and H. V. Poor, "6G internet of things: A comprehensive survey," *IEEE Internet Things J.*, vol. 9, no. 1, pp. 359–383, 2021.

[2] F. Guo, F. R. Yu, H. Zhang, X. Li, H. Ji, and V. C. Leung, "Enabling massive IoT toward 6G: A comprehensive survey," *IEEE Internet Things J.*, vol. 8, no. 15, pp. 11 891–11 915, 2021.

[3] K. Liu, X. Xu, M. Chen, B. Liu, L. Wu, and V. C. Lee, "A hierarchical architecture for the future internet of vehicles," *IEEE Commun. Mag.*, vol. 57, no. 7, pp. 41–47, 2019.

[4] M. N. Bhuiyan, M. M. Rahman, M. M. Billah, and D. Saha, "Internet of Things (IoT): A review of its enabling technologies in healthcare applications, standards protocols, security, and market opportunities," *IEEE Internet Things J.*, vol. 8, no. 13, pp. 10 474–10 498, 2021.

[5] Y. Xu, G. Gui, H. Gacanin, and F. Adachi, "A survey on resource allocation for 5G heterogeneous networks: Current research, future trends, and challenges," *IEEE Commun. Surveys Tuts.*, vol. 23, no. 2, pp. 668–695, 2021.

[6] A. Baghel, A. S. Parihar, V. Bhatia, K. Choi, and A. K. Mishra, "On joint impact of HPA non-linearity and imperfect SIC in NOMA enabled HCN using stochastic geometry," *IEEE Trans. Veh. Technol.*, pp. 1–14, 2024.

[7] C. Xu, B. Clerckx, S. Chen, Y. Mao, and J. Zhang, "Rate-splitting multiple access for multi-antenna joint radar and communications," *IEEE J. Sel. Topics Sig. Process.*, vol. 15, no. 6, pp. 1332–1347, 2021.

[8] J. A. Zhang, F. Liu, C. Masouros, R. W. Heath, Z. Feng, L. Zheng, and A. Petropulu, "An overview of signal processing techniques for joint communication and radar sensing," *IEEE J. Sel. Topics Signal Process.*, vol. 15, no. 6, pp. 1295–1315, 2021.

[9] F. Liu, Y. Cui, C. Masouros, J. Xu, T. X. Han, Y. C. Eldar, and S. Buzzi, "Integrated sensing and communications: Toward dual-functional wireless networks for 6G and beyond," *IEEE J. Sel. Areas Commun.*, vol. 40, no. 6, pp. 1728–1767, 2022.

[10] A. R. Chiriyath, B. Paul, G. M. Jacyna, and D. W. Bliss, "Inner bounds on performance of radar and communications co-existence," *IEEE Trans. Sig. Process.*, vol. 64, no. 2, pp. 464–474, 2015.

[11] Y. Liu, S. Zhang, X. Mu, Z. Ding, R. Schober, N. Al-Dhahir, E. Hossain, and X. Shen, "Evolution of NOMA toward next generation multiple access (NGMA) for 6G," *IEEE J. Sel. Areas Commun.*, vol. 40, no. 4, pp. 1037–1071, 2022.

[12] S. Hu, F. Rusek, and O. Edfors, "Beyond massive MIMO: The potential of data transmission with large intelligent surfaces," *IEEE Trans. Signal Process.*, vol. 66, no. 10, pp. 2746–2758, 2018.

[13] L. Dai, B. Wang, M. Wang, X. Yang, J. Tan, S. Bi, S. Xu, F. Yang, Z. Chen, M. Di Renzo *et al.*, "Reconfigurable intelligent surface-based wireless communications: Antenna design, prototyping, and experimental results," *IEEE access*, vol. 8, pp. 45 913–45 923, 2020.

[14] C. Pan, H. Ren, K. Wang, J. F. Kolb, M. Elkashlan, M. Chen, M. Di Renzo, Y. Hao, J. Wang, A. L. Swindlehurst *et al.*, "Reconfigurable intelligent surfaces for 6g systems: Principles, applications, and research directions," *IEEE Commun. Mag.*, vol. 59, no. 6, pp. 14–20, 2021.

[15] Y. Liu, X. Liu, X. Mu, T. Hou, J. Xu, M. Di Renzo, and N. Al-Dhahir, "Reconfigurable intelligent surfaces: Principles and opportunities," *IEEE Commun. Surveys Tuts.*, vol. 23, no. 3, pp. 1546–1577, 2021.

[16] C. Huang, A. Zappone, G. C. Alexandropoulos, M. Debbah, and C. Yuen, "Reconfigurable intelligent surfaces for energy efficiency in wireless communication," *IEEE Trans. Wireless Commun.*, vol. 18, no. 8, pp. 4157–4170, 2019.

[17] R. Deshpande, M. V. Katwe, K. Singh, and Z. Ding, "Resource allocation design for spectral-efficient URLLC using RIS-aided FD-NOMA system," *IEEE Wireless Commun. Lett.*, vol. 12, no. 7, pp. 1209–1213, 2023.

[18] K. Singh, F. Karim, S. K. Singh, P. K. Sharma, S. Mumtaz, and M. F. Flanagan, "Performance analysis of RIS-assisted full-duplex communications with infinite and finite blocklength codes," *IEEE Trans. Commun.*, vol. 71, no. 7, pp. 4262–4282, 2023.

[19] T. Van Chien, A. K. Papazafeiropoulos, L. T. Tu, R. Chopra, S. Chatzinotas, and B. Ottersten, "Outage probability analysis of irs-assisted systems under spatially correlated channels," *IEEE Wireless Commun. Lett.*, vol. 10, no. 8, pp. 1815–1819, 2021.

[20] H. Ibrahim, H. Tabassum, and U. T. Nguyen, "Exact coverage analysis of intelligent reflecting surfaces with Nakagami-m channels," *IEEE Trans. Veh. Technol.*, vol. 70, no. 1, pp. 1072–1076, 2021.

[21] Q. Tao, J. Wang, and C. Zhong, "Performance analysis of intelligent reflecting surface aided communication systems," *IEEE Commun. Lett.*, vol. 24, no. 11, pp. 2464–2468, 2020.

[22] A. M. Salhab and M. H. Samuh, "Accurate performance analysis of reconfigurable intelligent surfaces over Rician fading channels," *IEEE Wireless Commun. Lett.*, vol. 10, no. 5, pp. 1051–1055, 2021.

[23] Q. Wu and R. Zhang, "Towards smart and reconfigurable environment: Intelligent reflecting surface aided wireless network," *IEEE Commun. Mag.*, vol. 58, no. 1, pp. 106–112, 2019.

[24] C. Pradhan, A. Li, L. Song, J. Li, B. Vucetic, and Y. Li, "Reconfigurable intelligent surface (RIS)-enhanced two-way OFDM communications," *IEEE Trans. Veh. Technol.*, vol. 69, no. 12, pp. 16 270–16 275, 2020.

[25] L. Yang, J. Yang, W. Xie, M. O. Hasna, T. Tsiftsis, and M. Di Renzo, "Secrecy performance analysis of RIS-aided wireless communication systems," *IEEE Trans. Veh. Technol.*, vol. 69, no. 10, pp. 12 296–12 300, 2020.

[26] Z. Ding, L. Lv, F. Fang, O. A. Dobre, G. K. Karagiannidis, N. Al-Dhahir, R. Schober, and H. V. Poor, "A state-of-the-art survey on reconfigurable intelligent surface-assisted non-orthogonal multiple access networks," *Proc. IEEE*, vol. 110, no. 9, pp. 1358–1379, 2022.

[27] Z. Ding and H. V. Poor, "A simple design of IRS-NOMA transmission," *IEEE Commun. Lett.*, vol. 24, no. 5, pp. 1119–1123, 2020.

[28] X. Yue and Y. Liu, "Performance analysis of intelligent reflecting surface assisted NOMA networks," *IEEE Trans. Wireless Commun.*, vol. 21, no. 4, pp. 2623–2636, 2021.

[29] Z. Ding, R. Schober, and H. V. Poor, "On the impact of phase shifting designs on irs-noma," *IEEE Wireless Commun. Lett.*, vol. 9, no. 10, pp. 1596–1600, 2020.

[30] T. Hou, Y. Liu, Z. Song, X. Sun, Y. Chen, and L. Hanzo, "Reconfigurable intelligent surface aided NOMA networks," *IEEE J. Sel. Areas Commun.*, vol. 38, no. 11, pp. 2575–2588, 2020.

[31] A. Khaleel and E. Basar, "A novel NOMA solution with RIS partitioning," *IEEE J. Sel. Topics Signal Process.*, vol. 16, no. 1, pp. 70–81, 2021.

[32] L. Bariah, S. Muhaidat, P. C. Sofotasios, F. El Bouanani, O. A. Dobre, and W. Hamouda, "Large intelligent surface-assisted nonorthogonal multiple access for 6G networks: Performance analysis," *IEEE Internet Things J.*, vol. 8, no. 7, pp. 5129–5140, 2021.

[33] Y. Cheng, K. H. Li, Y. Liu, K. C. Teh, and G. K. Karagiannidis, "Non-orthogonal multiple access (NOMA) with multiple intelligent reflecting surfaces," *IEEE Trans. Wireless Commun.*, vol. 20, no. 11, pp. 7184–7195, 2021.

[34] B. Zheng, Q. Wu, and R. Zhang, "Intelligent reflecting surface-assisted multiple access with user pairing: NOMA or OMA?" *IEEE Commun. Lett.*, vol. 24, no. 4, pp. 753–757, 2020.

[35] Y. Cheng, K. H. Li, Y. Liu, K. C. Teh, and H. V. Poor, "Downlink and uplink intelligent reflecting surface aided networks: NOMA and OMA," *IEEE Trans. Wireless Commun.*, vol. 20, no. 6, pp. 3988–4000, 2021.

[36] X. Mu, Y. Liu, L. Guo, J. Lin, and N. Al-Dhahir, "Exploiting intelligent reflecting surfaces in noma networks: Joint beamforming optimization," *IEEE Trans. Wireless Commun.*, vol. 19, no. 10, pp. 6884–6898, 2020.

[37] S. K. Singh, K. Agrawal, K. Singh, C.-P. Li, and Z. Ding, "NOMA enhanced hybrid RIS-UAV-assisted full-duplex communication system with imperfect SIC and CSI," *IEEE Trans. Commun.*, vol. 70, no. 11, pp. 7609–7627, 2022.

[38] H. Wang, C. Liu, Z. Shi, Y. Fu, and R. Song, "On power minimization

for IRS-aided downlink NOMA systems," *IEEE Wireless Commun. Lett.*, vol. 9, no. 11, pp. 1808–1811, 2020.
[39] X. Mu, Z. Wang, and Y. Liu, "NOMA for integrating sensing and communications towards 6G: A multiple access perspective," *IEEE Wireless Commun.*, pp. 1–8, 2023.
[40] C. Zhang, W. Yi, Y. Liu, and L. Hanzo, "Semi-integrated-sensing-and-communication (Semi-ISaC): From OMA to NOMA," *IEEE Trans. Commun.*, vol. 71, no. 4, pp. 1878–1893, 2023.
[41] Z. Wang, Y. Liu, X. Mu, and Z. Ding, "NOMA inspired interference cancellation for integrated sensing and communication," in *IEEE Int. Conf. Commun.* IEEE, 2022, pp. 3154–3159.
[42] C. Ouyang, Y. Liu, and H. Yang, "Revealing the impact of SIC in NOMA-ISAC," *IEEE Wireless Communications Letters*, vol. 12, no. 10, pp. 1707–1711, 2023.
[43] C. Ouyang, Y. Liu, H. Yang, and N. Al-Dhahir, "Integrated sensing and communications: A mutual information-based framework," *IEEE Commun. Mag.*, vol. 61, no. 5, pp. 26–32, 2023.
[44] X. Wang, J. Han, S. Tian, D. Xia, L. Li, and T. J. Cui, "Amplification and manipulation of nonlinear electromagnetic waves and enhanced nonreciprocity using transmissive space-time-coding metasurface," *Adv. Sci.*, vol. 9, no. 11, p. 2105960, 2022.
[45] Z. Zhang, L. Dai, X. Chen, C. Liu, F. Yang, R. Schober, and H. V. Poor, "Active RIS vs. passive RIS: Which will prevail in 6G?" *IEEE Trans. Commun.*, vol. 71, no. 3, pp. 1707–1725, 2022.
[46] E. Basar and H. V. Poor, "Present and future of reconfigurable intelligent surface-empowered communications [perspectives]," *IEEE Signal Processing Mag.*, vol. 38, no. 6, pp. 146–152, 2021.
[47] K. Liu, Z. Zhang, L. Dai, S. Xu, and F. Yang, "Active reconfigurable intelligent surface: Fully-connected or sub-connected?" *IEEE Commun. Lett.*, vol. 26, no. 1, pp. 167–171, 2021.
[48] R. Liu, M. Li, H. Luo, Q. Liu, and A. L. Swindlehurst, "Integrated sensing and communication with reconfigurable intelligent surfaces: Opportunities, applications, and future directions," *IEEE Wireless Commun.*, vol. 30, no. 1, pp. 50–57, 2023.
[49] A. Fascista, M. F. Keskin, A. Coluccia, H. Wymeersch, and G. Seco-Granados, "RIS-aided joint localization and synchronization with a single-antenna receiver: Beamforming design and low-complexity estimation," *IEEE J. Sel. Topics Signal Process.*, vol. 16, no. 5, pp. 1141–1156, 2022.
[50] R. S. P. Sankar, S. P. Chepuri, and Y. C. Eldar, "Beamforming in integrated sensing and communication systems with reconfigurable intelligent surfaces," *IEEE Trans. Wireless Commun.*, vol. 23, no. 5, pp. 4017–4031, 2024.
[51] M. Hua, Q. Wu, C. He, S. Ma, and W. Chen, "Joint active and passive beamforming design for IRS-aided radar-communication," *IEEE Trans. Wireless Commun.*, vol. 22, no. 4, pp. 2278–2294, 2022.
[52] T. Guo, X. Li, M. Mei, Z. Yang, J. Shi, K.-K. Wong, and Z. Zhang, "Joint communication and sensing design in coal mine safety monitoring: 3-d phase beamforming for ris-assisted wireless networks," *IEEE Internet Things J.*, vol. 10, no. 13, pp. 11 306–11 315, 2023.
[53] X. Wang, Z. Fei, and Q. Wu, "Integrated sensing and communication for RIS-assisted backscatter systems," *IEEE Internet Things J.*, vol. 10, no. 15, pp. 13 716–13 726, 2023.
[54] Z. Xing, R. Wang, and X. Yuan, "Joint active and passive beamforming design for reconfigurable intelligent surface enabled integrated sensing and communication," *IEEE Trans. Commun.*, vol. 71, no. 4, pp. 2457–2474, 2023.
[55] Z. Wang, X. Mu, and Y. Liu, "STARS enabled integrated sensing and communications," *IEEE Trans. Wireless Commun.*, vol. 22, no. 10, pp. 6750–6765, 2023.
[56] X. Shao, C. You, W. Ma, X. Chen, and R. Zhang, "Target sensing with intelligent reflecting surface: Architecture and performance," *IEEE J. Sel. Areas Commun.*, vol. 40, no. 7, pp. 2070–2084, 2022.
[57] M. Elhattab, M.-A. Arfaoui, and C. Assi, "CoMP transmission in downlink NOMA-based heterogeneous cloud radio access networks," *IEEE Trans. Commun.*, vol. 68, no. 12, pp. 7779–7794, 2020.
[58] P. Swami, M. K. Mishra, V. Bhatia, T. Ratnarajah, and A. Trivedi, "Performance analysis of sub-6 GHz/mmWave NOMA hybrid-HetNets using partial CSI," *IEEE Trans. Veh. Technol.*, vol. 71, no. 12, pp. 12 958–12 971, 2022.
[59] T. Hou, Y. Liu, Z. Song, X. Sun, and Y. Chen, "MIMO-NOMA networks relying on reconfigurable intelligent surface: A signal cancellation-based design," *IEEE Trans. Commun.*, vol. 68, no. 11, pp. 6932–6944, 2020.
[60] E. Björnson, Ö. Özdogan, and E. G. Larsson, "Intelligent reflecting surface versus decode-and-forward: How large surfaces are needed to beat relaying?" *IEEE Wireless Commun. Lett.*, vol. 9, no. 2, pp. 244–248, 2019.
[61] R. Zhang, X. Hu, H. Liu, Y. Zhang, Z. Luo, and H. Wang, "Performance analysis for MIMO-NOMA systems with transceivers and group-wise SIC," *IEEE Trans. Veh. Technol.*, vol. 72, no. 12, pp. 16 221–16 235, 2023.
[62] Z. Ding, R. Schober, and H. V. Poor, "Unveiling the importance of SIC in NOMA systems—part 1: State of the art and recent findings," *IEEE Commun. Lett.*, vol. 24, no. 11, pp. 2373–2377, 2020.
[63] Z. Ding, F. Adachi, and H. V. Poor, "The application of MIMO to non-orthogonal multiple access," *IEEE Trans. Wireless Commun.*, vol. 15, no. 1, pp. 537–552, 2016.
[64] H. Liu, X. Yuan, and Y.-J. A. Zhang, "Matrix-calibration-based cascaded channel estimation for reconfigurable intelligent surface assisted multiuser MIMO," *IEEE J. Sel. Areas Commun.*, vol. 38, no. 11, pp. 2621–2636, 2020.
[65] Z. Yu, H. Ren, C. Pan, G. Zhou, B. Wang, M. Dong, and J. Wang, "Active RIS-aided ISAC systems: Beamforming design and performance analysis," *IEEE Trans. Commun.*, vol. 72, no. 3, pp. 1578–1595, 2024.
[66] J. G. Andrews, F. Baccelli, and R. K. Ganti, "A tractable approach to coverage and rate in cellular networks," *IEEE Trans. on Commu.*, vol. 59, no. 11, pp. 3122–3134, 2011.
[67] A. S. Parihar, P. Swami, V. Bhatia, and Z. Ding, "Performance analysis of SWIPT enabled cooperative-NOMA in heterogeneous networks using carrier sensing," *IEEE Trans. Veh. Technol.*, vol. 70, no. 10, pp. 10 646–10 656, 2021.
[68] M. K. Simon and M.-S. Alouini, "Digital communications over fading channels," *IEEE Trans. Inf. Theory*, vol. 54, no. 7, pp. 3369–3370, 2008.
[69] P. Swami, V. Bhatia, S. Vuppala, and T. Ratnarajah, "On user offloading in NOMA-HetNet using repulsive point process," *IEEE Syst. J.*, vol. 13, no. 2, pp. 1409–1420, 2018.
[70] Z. Xie, W. Yi, X. Wu, Y. Liu, and A. Nallanathan, "STAR-RIS aided noma in multicell networks: A general analytical framework with gamma distributed channel modeling," *IEEE Trans, Commun.*, vol. 70, no. 8, pp. 5629–5644, 2022.
[71] A. S. Parihar, P. Swami, and V. Bhatia, "On performance of SWIPT enabled PPP distributed cooperative NOMA networks using stochastic geometry," *IEEE Trans. Veh. Technol.*, vol. 71, no. 5, pp. 5639–5644, 2022.
[72] X. Yue, M. Song, C. Ouyang, Y. Liu, T. Li, and T. Hou, "Exploiting active RIS in NOMA networks with hardware impairments," *IEEE Trans. Veh. Technol.*, 2024.
[73] N. Bhargav, C. R. N. da Silva, Y. J. Chun, É. J. Leonardo, S. L. Cotton, and M. D. Yacoub, "On the product of two $\kappa-\mu$ random variables and its application to double and composite fading channels," *IEEE Trans. Wireless Commun.*, vol. 17, no. 4, pp. 2457–2470, 2018.
[74] I. S. Gradshteyn and I. M. Ryzhik, *Table of Integrals, Series, and Products*. 6th ed. New York, NY, USA: Academic Press, 2000.
[75] J. Stoer and R. Bulirsch, *Introduction to numerical analysis*. Springer Science & Business Media, 2013, vol. 12.

Abhinav Singh Parihar completed B.Tech from the National Institute of Technology, Raipur, India, in 2013. He worked as a Lecturer at Government Polytechnic College Rajgarh under the Directorate of Technical Education Madhya Pradesh till 2019. He received his Ph.D. degree from the Indian Institute of Technology Indore, India, in 2024. He is currently a Postdoctoral Fellow at the National Sun-Yet San University Kaohsiung, Taiwan. His current research interests include non-orthogonal multiple access, heterogeneous networks, stochastic geometry, multiple-input multiple-output, integrated sensing and communication, and reconfigurable intelligent surface-assisted communications.

Keshav Singh (Member, IEEE) received the Ph.D. degree in Communication Engineering from National Central University, Taiwan, in 2015. He currently works at the Institute of Communications Engineering, National Sun Yat-sen University (NSYSU), Taiwan as an Associate Professor. Prior to this, he held the position of Research Associate from 2016 to 2019 at the Institute of Digital Communications, University of Edinburgh, U.K. From 2019 to 2020, he was associated with the University College Dublin, Ireland as a Research Fellow. He chaired workshops on conferences like IEEE GLOBECOM 2023 and IEEE WCNC, 2024. He also serves as leading guest editor of IEEE Transactions on Green Communications and Networking Special Issue on Design of Green Near-Field Wireless Communication Networks and IEEE Internet of Things Journal Special Issue on Positioning and Sensing for Near-Filed (NF)-driven Internet-of-Everything. He leads research in the areas of green communications, resource allocation, transceiver design for full-duplex radio, ultra-reliable low-latency communication, non-orthogonal multiple access, machine learning for wireless communications, integrated sensing and communications, non-terrestrial networks, and large intelligent surface-assisted communications.

Vimal Bhatia (Senior Member, IEEE) received the Ph.D. degree from the Institute for Digital Communications, The University of Edinburgh, Edinburgh, U.K., in 2005. He is currently a Professor with the Indian Institute of Technology (IIT) Indore, India. He is also an Adjunct Faculty Member with IIT Delhi and IIIT Delhi, India. During the Ph.D. degree, he also received the IEEE Fellowship for collaborative research with the Department of Systems and Computer Engineering, Carleton University, Canada. He is also a DRISHTI CPS Chair Professor with IIT Indore. He is also with the School of Electronic and Information Engineering, Soochow University, China, as an Honorary Chair Professor. He is also a Young Faculty Research Fellow with MeitY, Government of India. He was with various IT companies for over 11 years both in India and U.K. He is a PI/Co-PI/Coordinator for external projects with funding of over U.S. 20 million from MeitY, DST, UKIERI, MoE, AKA, IUSSTF, and KPMG. He has more than 350 peer-reviewed publications and has filed 13 patents (with five granted). He is an IEEE, Elsevier, Wiley, Springer, and IET reviewer. He is a fellow of IETE and OSI and a certified SCRUM Master. He was a recipient of the Prof SVC Aiya Memorial Award, in 2019. He was also the General Co-Chair of IEEE ANTS 2018 and the General Vice-Chair of IEEE ANTS 2017. He was the Founder and the Head of the Center for Innovation and Entrepreneurship, the Associate Dean of Research and Development, and the Dean of Academic Affairs. He has delivered many talks and tutorials, conducted faculty development programs for the World Bank's NPIU TEQIP-III, and was invited to talk at WWRF46- Paris. He is also an Associate Editor of IETE Technical Review, Frontiers in Communications and Networks, Frontiers in Signal Processing, IEEE WIRELESS COMMUNICATIONS LETTERS, and IEEE TRANSACTIONS ON GREEN COMMUNICATIONS AND NETWORKING. He is a current member of the Steering Committee of IEEE ANTS. He has been mentioned among the World's Top 2% Scientists by Stanford University.

Chih-Peng Li (Fellow, IEEE) received the B.S. degree in Physics from National Tsing Hua University, Hsin Chu, Taiwan, and the Ph.D. degree in Electrical Engineering from Cornell University, NY, USA. Dr. Li was a Member of the Technical Staff with Lucent Technologies. Since 2002, he has been with National Sun Yat-sen University (NSYSU), Kaohsiung, Taiwan, where he is currently a Distinguished Professor. Dr. Li has served in various positions with NSYSU, including the Chairman of the Electrical Engineering Department, the VP of General Affairs, the Dean of Engineering College, and the VP of Academic Affairs. His research interests include wireless communications, baseband signal processing, and data networks. He is now the Director General of the Engineering and Technologies Department, at the National Science and Technology Council, Taiwan. Dr. Li is currently the Chapter Chair of the IEEE Broadcasting Technology Society Tainan Section. Dr. Li has also served as the Chapter Chair of the IEEE Communication Society Tainan Section, the President of the Taiwan Institute of Electrical and Electronics Engineering, the Editor of IEEE Transactions on Wireless Communications, the Associate Editor of IEEE Transactions on Broadcasting, and the Member of Board of Governors with IEEE Tainan Section. Dr. Li has received various awards, including the Outstanding Research Award from the Ministry of Science and Technology. Dr. Li is a Fellow of the IEEE.

Trung Q. Duong (Fellow, IEEE) is a Canada Excellence Research Chair (CERC) and a Full Professor at Memorial University, Canada. He is also the adjunct Chair Professor in Telecommunications at Queen's University Belfast, UK and a Research Chair of Royal Academy of Engineering, UK. He was a Distinguished Advisory Professor at Inje University, South Korea (2017-2019), an Adjunct Professor and the Director of Institute for AI and Big Data at Duy Tan University, Vietnam (2012-present), and a Visiting Professor (under Eminent Scholar program) at Kyung Hee University, South Korea (2023-2025). His current research interests include quantum communications, wireless communications, quantum machine learning, and quantum optimisation.

Dr. Duong has served as an Editor/Guest Editor for the IEEE TRANSACTIONS ON WIRELESS COMMUNICATIONS, IEEE TRANSACTIONS ON COMMUNICATIONS, IEEE TRANSACTIONS ON VEHICULAR TECHNOLOGY, IEEE COMMUNICATIONS LETTERS, IEEE WIRELESS COMMUNICATIONS LETTERS, IEEE WIRELESS COMMUNICATIONS, IEEE COMMUNICATIONS MAGAZINES, and IEEE JOURNAL ON SELECTED AREAS IN COMMUNICATIONS. He received the Best Paper Award at the IEEE VTC-Spring 2013, IEEE ICC 2014, IEEE GLOBECOM 2016, 2019, 2022, IEEE DSP 2017, IWCMC 2019, 2023, and IEEE CAMAD 2023. He has received the two prestigious awards from the Royal Academy of Engineering (RAEng): RAEng Research Chair (2021-2025) and the RAEng Research Fellow (2015-2020). He is the recipient of the prestigious Newton Prize 2017.